Acta Pharmaceutica Sinica B 2024;14(7):3086−3109

Chinese Pharmaceutical Association
Institute of Materia Medica, Chinese Academy of Medical Sciences

Acta Pharmaceutica Sinica B

www.elsevier.com/locate/apsb
www.sciencedirect.com

ORIGINAL ARTICLE

Deep simulated annealing for the discovery of novel dental anesthetics with local anesthesia and anti-inflammatory properties

Yihang Hao[a,†], Haofan Wang[a,†], Xianggen Liu[b,†], Wenrui Gai[c,†], Shilong Hu[c], Wencheng Liu[c], Zhuang Miao[c], Yu Gan[c], Xianghua Yu[a], Rongjia Shi[a], Yongzhen Tan[a], Ting Kang[c], Ao Hai[c], Yi Zhao[c], Yihang Fu[a], Yaling Tang[a], Ling Ye[a], Jin Liu[c], Xinhua Liang[a,*], Bowen Ke[c,*]

[a]*State Key Laboratory of Oral Diseases and National Clinical Research Center for Oral Diseases, West China Hospital of Stomatology, Sichuan University, Chengdu 610041, China*
[b]*College of Computer Science, Sichuan University, Chengdu 610065, China*
[c]*Department of Anesthesiology, Laboratory of Anesthesia and Critical Care Medicine, National-Local Joint Engineering Research Centre of Translational Medicine of Anesthesiology, Frontiers Science Center for Disease-Related Molecular Network, West China Hospital, Sichuan University, Chengdu 610041, China*

Received 22 November 2023; received in revised form 4 January 2024; accepted 22 January 2024

KEY WORDS

Multifunctional drugs;
Deep simulated annealing;
Molecule generation;
Articaine derivatives;
AI-enhanced drug discovery

Abstract Multifunctional therapeutics have emerged as a solution to the constraints imposed by drugs with singular or insufficient therapeutic effects. The primary challenge is to integrate diverse pharmacophores within a single-molecule framework. To address this, we introduced DeepSA, a novel edit-based generative framework that utilizes deep simulated annealing for the modification of articaine, a well-known local anesthetic. DeepSA integrates deep neural networks into metaheuristics, effectively constraining molecular space during compound generation. This framework employs a sophisticated objective function that accounts for scaffold preservation, anti-inflammatory properties, and covalent constraints. Through a sequence of local editing to navigate the molecular space, DeepSA successfully identified **AT-17**, a derivative exhibiting potent analgesic properties and significant anti-inflammatory activity in various animal models. Mechanistic insights into **AT-17** revealed its dual mode of action: selective inhibition of $Na_V1.7$ and 1.8 channels, contributing to its prolonged local anesthetic effects,

*Corresponding authors.
E-mail addresses: lxh88866@scu.edu.cn (Xinhua Liang), bowenke@scu.edu.cn (Bowen Ke).
[†]These authors made equal contributions to this work.

Peer review under the responsibility of Chinese Pharmaceutical Association and Institute of Materia Medica, Chinese Academy of Medical Sciences.

https://doi.org/10.1016/j.apsb.2024.01.019

and suppression of inflammatory mediators *via* modulation of the NLRP3 inflammasome pathway. These findings not only highlight the efficacy of **AT-17** as a multifunctional drug candidate but also highlight the potential of DeepSA in facilitating AI-enhanced drug discovery, particularly within stringent chemical constraints.

1. Introduction

The paradigm shift towards multifunctional drugs signifies a promising advancement in enhancing the safety and efficacy of pharmacological treatments, as supported by an emerging body of evidence[1]. Traditional monofunctional drugs that are effective in certain contexts often fail to provide satisfactory therapeutic efficacy. However, the advent of multifunctional drugs introduces significant complexities, particularly when augmenting a ligand initially designed for a singular function with additional therapeutic capabilities. A critical challenge in this development is ensuring that the integration of new pharmacophores does not diminish the original ligand activity. Current strategies in multifunctional drug development are predominantly based on rational design, employing techniques such as merged pharmacophores and linked pharmacophore models. Recent reviews have provided extensive insights into the current state-of-the-art in this field[2,3]. Despite these strides, the field continues to grapple with challenges in target combinations, ligand selection, balancing of activities, and optimization of physicochemical properties. A notable gap lies in the development of molecules with innovative activity profiles based on existing structural bases.

In response to these challenges, generative deep learning (GDL) has emerged as a novel approach in molecular generation and drug design[4-7], utilizing neural networks, GDL modes as variational autoencoders (VAEs)[8], generative adversarial networks (GANs)[9], flow-based generative networks[10], and diffusion models[11], which have demonstrated proficiency in learning data distributions in a comprehensive end-to-end manner[12]. The emergence of transformer architectures and graph neural networks has further expanded GDL's capabilities, specifically capturing the intricate structures and interrelationships of molecules[13,14]. Nevertheless, these models predominantly focus on generating single-activity targeted molecules, a limitation that stems partly from the intricate objectives of multifunctional drug development. This complexity reduces the feasible solution space and complicates the balance between multiple targets and activities during the generation process. Furthermore, the scarcity of successful examples of multifunctional drugs impedes the training and refinement of GDL models.

In this study, we propose DeepSA, a novel deep-simulated annealing framework. This approach effectively integrates sophisticated pre-trained neural networks into metaheuristics to constrain the search space for generating multifunctional molecules. DeepSA utilizes simulated annealing (SA), a heuristic search algorithm aimed at a flexibly defined objective function[15] tailored through a complex objective function encompassing scaffold preservation, anti-inflammatory properties, and covalent validity. Through iterative local editing processes—atom replacement, insertion, deletion, and cyclization—DeepSA proposes potential structure editing and then accepts or rejects the proposal based on the returned objective function score. Generally, a molecule with a higher score is accepted, whereas a molecule with a lower score has a higher probability of being rejected. This process is controlled by the annealing temperature to strategically modulate the exploration of the search space less greedily. A message-passing neural network edits content, thereby controlling the quality of editing during the generation process.

We used the DeepSA to develop novel local anesthetics with multiple activities. Local anesthesia is indispensable for pain management. However, their effectiveness and duration are notably diminished under inflammatory conditions. Notably, the success rate of anesthesia in mandibular teeth with irreversible pulpitis exceeds 73%[16,17]. Attempts to enhance anesthetic efficacy through drug combinations[18] have yielded limited improvements and have been concomitant with potential side effects due to additional components. Articaine, which is characterized by its unique thiophene ring structure, is the predominant local anesthetic used in dental practice[19,20]. Using the structural foundation of articaine, DeepSA generated over 400 analogs that fulfilled the pre-defined criteria and exhibited enhanced anti-inflammatory scores compared to articaine. Among these, a standout compound, **AT-17**, not only demonstrated pronounced anesthetic effects but also augmented safety profiles in diverse animal models. Molecular dynamics simulations and electrophysiological techniques were used to elucidate the underlying mechanisms of **AT-17,** the local anesthetic and anti-inflammatory actions. These data suggest that **AT-17** is a promising candidate for a novel local dental anesthetic.

2. Results and discussion

2.1. Virtual screening based on deep learning models

We present a deep-simulated annealing (SA) approach, termed DeepSA, for generating molecules with multiple activities. This methodology synergizes advanced neural network capabilities with metaheuristic algorithms to restrict the search space for discrete optimization tasks. DeepSA searches the discrete structural space of molecules towards a specific pre-defined objective through a series of local edits using SA (Fig. 1). For DeepSA, we extended our preliminary work[21] to consider cyclization in the editing operations of structures capable of atom replacement, insertion, deletion, and cyclization. In particular, we introduce the generation process of DeepSA in detail (Algorithm 1). Given an input molecule x_0, DeepSA searches from the molecule space to maximize the pre-defined objective $f(\cdot)$. The DeepSA starts at x_0 itself. For each step t, DeepSA randomly selects a search action (*i.e.*, atom insertion, deletion, replacement, and cyclization) at a

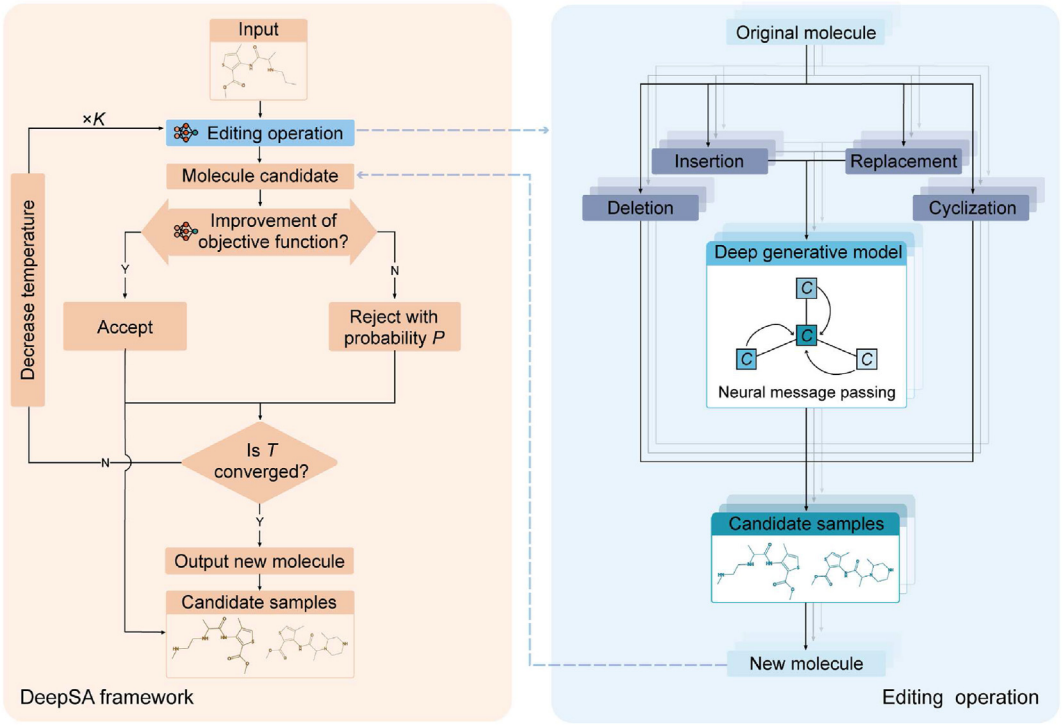

Figure 1 The DeepSA framework. DeepSA accepts an arbitrary molecule structure (*e.g.*, articaine) as input and generate molecules by performing a sequence of local editing steps, namely, atom replacement, insertion, deletion and cyclization.

position k; if insertion or replacement is selected, DeepSA also proposes a candidate atom such that a candidate molecule x_* is formed. If the new candidate x_* achieves a better score, *i.e.*, $f(x_*) > f(x_t)$, then DeepSA can promptly approve the proposal. Otherwise, the acceptance probability $e^{\frac{f(x_*)>f(x_t)}{T}}$ is governed by the current annealing temperature. In other words, the probability of accepting the proposal is determined by Eq. (1). The candidate molecule x_{t+1} for the next step becomes x_* if the proposal is accepted or remains x_t if the proposal is rejected. Until the maximum search iterations, we collected the generated molecules that had better objective values than the input molecules. The primary distinction between DeepSA and traditional pharmacophore-based virtual screening lies in that our approach advocates for content editing, thereby enabling precise control over the editing quality throughout the generation process.

Algorithm 1: The DeepSA framework

1. **Input**: Original sample x_0
2. **for** $t \in \{1, \ldots, N\}$ **do**
3. Randomly selects an editing operation and a position k
4. Edits the current sample x_t at position k
5. Rank the modified samples and select a candidate x_*
6. Compute the accepting probability P_{accept} by Eq. (1)
7. With probability P_{accept}, $x_{t+1} = x_*$
8. With probability $1 - P_{\text{accept}}$, $x_{t+1} = x_t$
9. $T = \max(0, T_{\text{init}} - C \cdot t)$
10. **end for**

$$P(\text{accept}|x_*, x_t, T) = \min\left(1, e^{\frac{f(x_*)>f(x_t)}{T}}\right) \quad (1)$$

Temperature plays a crucial role as it dictates the acceptance probability of a new candidate. We employ a linear annealing schedule, expressed as $T = \max(0, T_{\text{init}} - C \cdot t)$, where T_{init} represents the initial temperature and C is the decreasing rate. At the beginning, the temperature T is set high, leading to a high acceptance probability even if x_* is worse than x_t. The high temperature encourages the model to explore the chemical space thoroughly. Subsequently, the temperature gradually decreases, allowing the model to converge to a specific optimum. See Section Experimental for more implementation details of DeepSA.

To evaluate the generation performance of DeepSA, we apply it to generate the molecules with higher molecular solubility. Following Jin et al.[22], 800 molecules in ZINC250K with the lowest scores were used as the initial molecules of DeepSA. We compared DeepSA with multiple advanced generative methods, including junction tree VAE (JT-VAE)[22], GCPN[23], JADE[24], MMPA[25], MoFlow[26], and GraphAF[27]. In particular, GraphAF leverages graph neural networks to produce the molecules by reinforcement learning. In this comparison, the scaffold constraints were considered to preserve the key functional groups of the given molecules, which were divided into four groups (with similarity thresholds). Supporting Information Table S1 reported the property improvements and the success rates of the deep generative models. The success rates are computed by the proportion of the generated molecules that have higher property values than the initial ones. In comparison, JT-VAE obtains the worse generation performance, showing the difficulty of learning a robust latent space of molecules. RL-based methods, such as GCPN and GraphAF, present better generation results but still lag

behind DeepSA by a large margin. We observed that the success rate of DeepSA is not 100%, indicating that DeepSA may sometimes fail to produce better molecules. We could address this issue by repeated sampling. Overall, the impressive performances of DeepSA in four types of scaffold constraints reflected that DeepSA is a powerful molecule generation method in computer-aided drug design.

Next, we applied DeepSA to develop novel local anesthetics with anti-inflammatory activity. First, we designed a sophisticated objective function that considers the anti-inflammatory score, scaffold constraints, and valency validity. We then collected 22,165 bioassay data points from the AICD[28] and trained an anti-inflammatory predictor based on them. The bioactivity values are the inhibitor constants (K_i) recorded according to the actual bioassay models and are normalized on a logarithmic scale, where $P = -\log 10\,(\cdot)$. The predictor was a three-layer message-passing neural network[29] trained using 90% of the bioassay data. The remaining 10% of the data points were unseen by the anti-inflammatory predictor and were used for the performance evaluation. The overall test RMSE was 0.87, with a Pearson correlation coefficient of 0.82. These results indicate that the predictor can accurately predict the anti-inflammatory properties. For a newly generated molecule x_*, its anti-inflammatory score can be calculated by function f_p, $f_p(x_*) = Mf_{\text{score}}(x_*)$, and M is a hyper-parameter. In addition to the anti-inflammatory predictor in the objective function, we also leveraged the chemically relevant scaffold of articaine as a structural constraint and used covalence validity to guide the molecule search, given by Eq. (2).

$$\text{Validity}(x_*, x_0) = f_g(x_*) \cdot 1_{\{f_{\text{scaffold}}(x_*, x_0)\}} \tag{2}$$

where the function f_g indicates whether the sample x_* is subject to the valency conditions of the molecules or not, which can be directly calculated by RDKit package. Where $1_{\{\cdot\}}$ is an indicator function that yields 1 when its argument is true, and 0 otherwise. If x_* and x_0 (articaine) have a same scaffold, which can be calculated by RDKit package, $f_{\text{scaffold}}(x_*, x_0)$ returns true. In other words, a newly generated molecule is regarded as valid only if its grammar is correct and it shares a same scaffold with articaine. Finally, we combine these two functions and define the objective of DeepSA for molecule generation as a piecewise function, given by Eq. (3).

$$f(x_*) = \begin{cases} f_p(x_*), \text{if} & \text{Validity}(x_*, x_0) > 0 \\ -\infty, \text{if} & \text{Validity}(x_*, x_0) \le 0 \end{cases} \tag{3}$$

Overall, we obtained more than 400 analogs that satisfied these constraints and possessed higher anti-inflammatory scores than articaine alone. To obtain potentially active molecules with optimal medicinal properties, we utilized ADMETlab 2.0, which is an integrated platform for comprehensive ADMET property prediction[30]. The screening criteria were specifically tailored for local anesthetics in stomatology with an emphasis on drug-like properties, synthesizability, and cardiotoxicity (QED >0.5, rotor <10, donorHB <5, accptHB <10, hERG = 0, SAscore <0.35). Molecular docking screening with potential analgesia targets $Na_V1.7$ and $Na_V1.8$ was conducted using CDOCKER in Discovery Studio 2019. Based on the combined assessment of drug-like properties and docking scores, nine derivatives of articaine were found to be superior. For ring-opening compounds, chain flexibility may reduce binding efficiency, which should be properly considered in structure-activity studies. Considering its synthetic accessibility and scope of structural exploration, **AT-1** was identified as a lead compound (Fig. 2).

2.2. Chemistry

The synthetic routes and protocols for articaine (**AT**) derivatives are illustrated in Scheme 1. In general, a commercially available thiophene substrate (**1**) was coupled with different acyl bromides through acylation to afford intermediates **2a**−**c**. Then, the compound **AT-1-Boc** applied *N*-boc-piperazine for nucleophilic substitution with intermediate **2a** and reacted with hydrogen chloride 1,4-dioxane to form the desired product **AT-1**. Additionally, *N*-boc-piperazine (**3**) was substituted with suitable bromides and transformed into functionalized intermediates **4a**−**e** using TFA. Next, intermediates **2a**−**c** were smoothly substituted with diverse secondary amines bearing nitrogen-containing heterocycles to obtain **AT-2**−**26**. These reactions were mild and proceeded efficiently in moderate to good yields (mostly 50%−90%). Additionally, **AT** was hydrolyzed with sodium hydroxide and re-esterified to obtain **AT-27**−**30**. Finally, considering the water solubility and stability of the **AT** derivatives, all compounds in this study were prepared as hydrochloric acid salts for subsequent studies, which is consistent with the preparation of **AT** in the clinical.

2.3. Binding affinity of sodium ion channels in vitro

Sodium ion channel binding affinity was evaluated using cell membrane chromatography (CMC). This technique is more convenient for studying ligand−receptor interactions because it maintains the active conformation of the transmembrane protein and its biological activity[31,32]. CMC for $Na_V1.7$ and $Na_V1.8$ were prepared to evaluate the binding affinity of $Na_V1.7$ and $Na_V1.8$ related to local anesthesia, and CMC for $Na_V1.5$ was also prepared to reflect potential cardiac toxicity. The capacity factor (k') was used to screen drug-protein interactions[33] and was calculated using the following Eq. (4):

$$k' = (t_R - t_0) / t_0 \tag{4}$$

t_R refers to the retention time of the ligands, and t_0 refers to the retention time of the solvent. The retention time was detected by an ultraviolet online detector at 254 nm. A larger k' value refers to a stronger affinity between drugs and the membrane receptor; $k' < 0$ indicates no binding affinity and is labeled as $k' = 0$.

Based on the recommendation of **AT-1** by virtual screening, the Na_V binding affinity of the R_2 group was first explored to validate the necessity of the piperazine ring, as many results have indicated that rings influence the bioactivity of compounds[34]. As shown in Table 1, replacing piperazine with piperidine (**AT-3**) significantly decreased the affinity for $Na_V1.7$. Additionally, the morpholine derivative (**AT-5**), thiomorpholine (**AT-9**), and its dioxide derivative (**AT-10**) showed poor binding potency to $Na_V1.7$ and $Na_V1.8$. These results indicate the importance of piperazine (Table 2).

Focusing on the impact of the R_4 group on Na_V binding affinity, we observed that methyl (**AT-11**) and isopropyl (**AT-13**) substitutions in **AT-1** maintained $Na_V1.7$ affinity without significantly affecting $Na_V1.5$. Notably, the *tert*-butyl derivative (**AT-15**) showed a marked decrease in affinity for both $Na_V1.7$ and $Na_V1.8$, along with increased potential toxicity mediated by $Na_V1.5$, similar to the benzene derivative (**AT-18**). These findings highlight

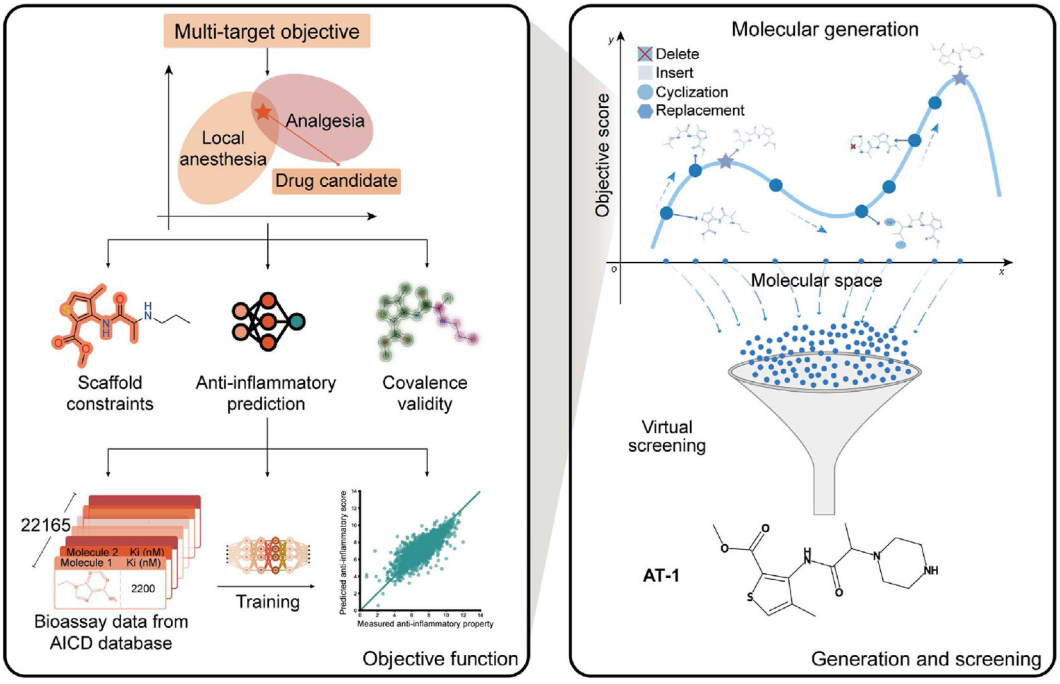

Figure 2 The generation process of the lead compound **AT-1** using DeepSA. The molecular generation was guided by the multi-function objective of local anesthesia and anti-inflammatory scores. DeepSA produces over 400 molecules and virtual screening was applied to identify **AT-1** based on the cardiotoxicity, membrane permeability and molecular docking score.

the crucial role of the spatial hindrance of the R_4 group in the binding affinity. Remarkably, the *n*-butyl derivative (**AT-17**) exhibited the highest affinity for both $Na_V1.7$ and $Na_V1.8$, with slightly reduced $Na_V1.5$ toxicity compared to **AT** and **AT-1**. The introduction of oxygen atoms (**AT-19** and **AT-20**) significantly escalated $Na_V1.5$ toxicity. Investigating the steric hindrance of the linker, we found that methyl (**AT-13**) and ethyl (**AT-22**) substitutions ensured efficient $Na_V1.7$ and $Na_V1.8$ binding compared to **AT-21**.

To explore the effects of the flexible ring-opening compounds generated by DeepSA, we examined substitutions on the clinical **AT** skeleton, focusing on the branched chain R_2 and R_3 groups (Table 3). When these were replaced with hydroxyl or ether groups (**AT-23**−**25**), the resulting compounds lost their ability to bind $Na_V1.7$. Interestingly, **AT-26** displayed an enhanced affinity for both $Na_V1.7$ and $Na_V1.5$, indicating that morpholine linked by branched chains might not be the optimal choice. Our analysis also showed that conformational restriction was crucial for improving the binding on $Na_V1.7$ and $Na_V1.8$, but not of $Na_V1.5$. In addition, we explored the modifications of the methyl ester, which is known to undergo rapid hydrolysis[35]. Remarkably, as the steric hindrance increased up to *n*-propyl (**AT-28**), binding to $Na_V1.7$ improved before decreasing again. The isopropyl-substituted variant (**AT-30**) not only lost $Na_V1.7$ binding ability but also exhibited increased cardiac toxicity by affecting $Na_V1.5$.

2.4. *In vivo screening*

Using the cutaneous trunci pinprick model[36], we evaluated the effects of subcutaneous infiltration of novel derivatives, each at a concentration of 62.3 mmol/L, equivalent to half the clinical concentration of **AT**. This concentration ensured local anesthesia in the rats without adverse reactions. The results illustrated in Fig. 3A revealed that the subcutaneous infiltration durations for **AT-1** (240 min), **AT-11** (260 min), **AT-13** (275 min), **AT-17** (400 min), and **AT-22** (260 min) were significantly longer than **AT** (120 min). Notably, these effective compounds were piperazine derivatives, aligned with their binding affinities to $Na_V1.7$ and $Na_V1.8$. Interestingly, **AT-15,** with a duration of 205 min, also demonstrated substantial efficacy despite its lower binding affinity in the CMC experiment. In contrast, piperidine and morpholine derivatives did not outperform piperazine derivatives. The AUC statistics further support these findings (Fig. 3B). Additionally, **AT-21** showed fewer effects than **AT**, correlating with its lower Na_V binding affinity. Ring-opening compounds undergo subcutaneous infiltration, indicating the importance of conformational restrictions. Unfortunately, compounds **AT-27**−**30** were excluded from further evaluation due to their systemic toxicity in rats, despite the high Na_V binding affinity of **AT-28**, possibly due to the slow hydrolysis of large ester groups, leading to drug accumulation. In summary, we identified **AT-1**, **AT-11**, **AT-13**, **AT-15**, **AT-17**, and **AT-22** as candidates for further assessments.

A sciatic nerve block model[37-39] was used to evaluate and compare the nerve-blocking effects of **AT** and its derivatives. After injection into the sciatic nerve of rats, sensory and motor functions were assessed using the hotplate test and extensor postural thrust (EPT) reaction test. The results indicated that **AT-13** (145 min), **AT-15** (190 min), **AT-17** (200 min), and **AT-22** (220 min) significantly extended the duration of effective sensory blockade compared with **AT** (Fig. 3C). For motor block, **AT-13** (140 min), **AT-15** (210 min), **AT-17** (260 min), and **AT-22** (240 min) outperformed **AT** (90 min), as shown in Fig. 3D. Overall, **AT-13**, **AT-15**, **AT-17**, and **AT-22** demonstrated superior nerve-blocking anesthetic effects, although there was no significant difference in sensory or motor blockade between these compounds.

Therefore, the anti-inflammatory effects of these compounds should be investigated. We established a model of chronic inflammation induced by complete Freund's adjuvant (CFA) [40].

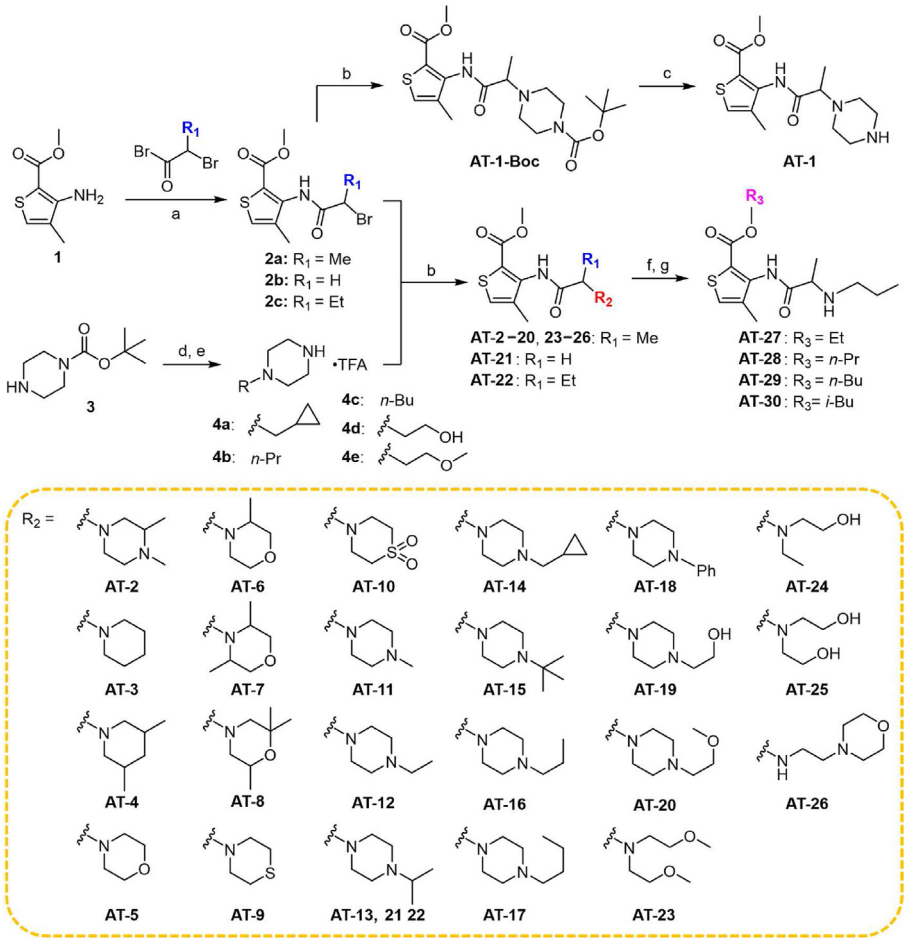

Scheme 1 Reagents and conditions: (a) acyl bromide, K_2CO_3, dichloromethane (DCM), −20 °C to rt; (b) suitable amines, K_2CO_3, *N*,*N*-dimethylformamide (DMF), rt or 50 °C; (c) hydrogen chloride (in 1,4-dioxane), rt; (d) suitable bromides, acetonitrile (CH_3CN), rt; (e) trifluoroacetic acid (TFA), DCM, rt; (c, f) 10 % NaOH, MeOH, 50 °C; (d, g) bromides, $NaHCO_3$, DMF, 50 °C.

Despite other compounds showing promise in previous studies, their efficacy is significantly reduced during inflammation. Notably, only **AT-17** (83.3 min) maintained a longer duration of action under these conditions, markedly outperforming **AT** (30 min) (Fig. 3E and F). In the acute inflammation model through a plantar incision[41], **AT** underperformed, whereas **AT-13** and **AT-17** demonstrated improved results, which is consistent with the findings from the CFA model (Fig. 3G and H).

2.5. *Pharmacodynamic evaluation of **AT-17** in orofacial pain models*

These results identified **AT-17** as a superior local anesthetic, guiding its focus in future research. To assess the effectiveness of **AT-17** in dental procedures, we employed orofacial pain models such as dental pulp injury, gingival incision, and tooth extraction (Fig. 4A). We evaluated anesthetic effectiveness by monitoring postoperative changes in food intake, body weight, and frequency of facial grooming. In the dental pulp injury model (Fig. 4B), **AT** and **AT-17** demonstrated similar face grooming frequencies, suggesting comparable anesthetic intensities; however, **AT-17** was more effective in reducing weight loss and pain-related decreases in food intake. In the gingival incision model (Fig. 4C), both **AT** and **AT-17** significantly lowered the face grooming frequency, with **AT-17** showing markedly better performance and a more pronounced recovery in body weight and food intake. The tooth extraction model (Fig. 4D) echoed these findings, with **AT-17** significantly mitigating weight loss and food intake. In the dental pulp injury model and tooth extraction model, the observation of facial grooming frequency occurs during the onset of anesthesia. This result only indicates that both compounds have effective anesthesia effects and cannot be used to compare the differences in anesthesia potency between the two groups. Therefore, it is possible that there may be no statistically significant difference between the **AT** group and the **AT-17** group. Overall, the results highlight the superior efficacy of **AT-17** in alleviating oral surgery-induced eating disruptions compared to **AT**.

2.6. *Electrophysiology of **AT-17***

To explore the anesthetic mechanism of **AT-17**, we investigated its effects on sodium channels, which are key targets for local anesthesia. Using whole-cell patch clamp techniques, we assessed the inhibitory effects of **AT** and **AT-17** on Na_V currents in rat dorsal root ganglion (DRG) and trigeminal neuron (TG) neurons. We observed a dose-dependent reduction in the peak current

Table 1 The Na_V binding affinity of the R_2 group.

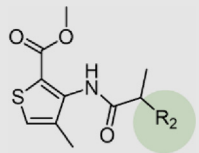

Compd.	R_2	k'			Compd.	R_2	k'		
		$Na_V1.7$	$Na_V1.8$	$Na_V1.5$			$Na_V1.7$	$Na_V1.8$	$Na_V1.5$
AT	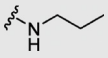	33	51	63	**AT-6**		12	15	28
AT-1	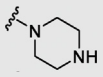	59.2	32	80.8	**AT-7**		5.8	12	24
AT-2	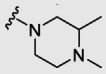	74.2	3.2	92	**AT-8**	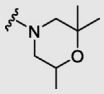	5.8	44	36.8
AT-3		10.6	37	1.1	**AT-9**		6.8	12.8	48.6
AT-4	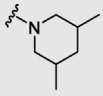	77	43	71.2	**AT-10**	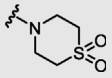	0	0.4	0
AT-5		4.8	11	18.4					

amplitude for both compounds. Notably, the IC_{50} of **AT-17** was 31.60 ± 2.07 μmol/L in DRG neurons and 23.63 ± 1.11 μmol/L in TG neurons, substantially lower than that of **AT** (71.24 ± 3.06 μmol/L and 34.66 ± 1.17 μmol/L, respectively), indicating stronger inhibition (Fig. 5A and B, Supporting Information Fig. S2A and S2B). Further experiments were conducted using HEK293T cells expressing $Na_V1.7$, $Na_V1.8$, or $Na_V1.5$. **AT-17** showed more potent inhibition of $Na_V1.7$ and $Na_V1.8$, with lower IC_{50} values than **AT**, suggesting superior efficacy. **AT-17** exhibits a higher IC_{50} value for $Na_V1.5$, indicating its selective inhibition and potentially enhanced cardiac safety (Fig. 5D−F).

We continued to record the action potentials evoked by depolarizing currents in the DRG neurons. Neither **AT-17** nor **AT** altered the resting membrane potential (RMP), indicating their effects were specific to sodium channels and did not affect the

Table 2 The Na_V binding affinity of the R_4 group and the linker.

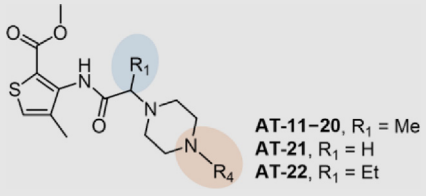

Compd.	R_4	k'			Compd.	R_4	k'		
		$Na_V1.7$	$Na_V1.8$	$Na_V1.5$			$Na_V1.7$	$Na_V1.8$	$Na_V1.5$
AT-11	Me	83.2	49	8	**AT-17**	*n*-Bu	163	122	22.4
AT-12	Et	4.6	43	1.2	**AT-18**	Ph	29.2	45	57.8
AT-13	*i*-Pr	94	55	23.2	**AT-19**		4.6	41	92
AT-14		5.4	115	22	**AT-20**		107	67	92
AT-15	*t*-Bu	0.2	0	116.4	**AT-21**	*i*-Pr	3	1.4	5.8
AT-16	*n*-Pr	6	55	42.4	**AT-22**	*i*-Pr	82.6	63	21.4

Table 3 The Na_V binding affinity of the R_2 and R_3 group.

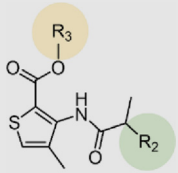

AT-23–30

Compd.	R_2	R_3	k'		
			$Na_V1.7$	$Na_V1.8$	$Na_V1.5$
AT-23	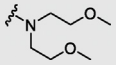	Me	14	2.6	43.6
AT-24	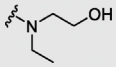	Me	0	3.0	27.6
AT-25	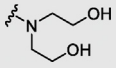	Me	0	1.2	12.1
AT-26	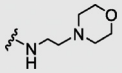	Me	104.2	44	72.4
AT-27	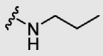	Et	52.8	23	0.6
AT-28	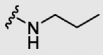	*n*-Pr	81.4	29	38
AT-29	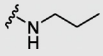	*n*-Bu	73	26	35
AT-30	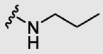	*i*-Bu	4.4	0	105.4

potassium channels (Fig. 5G). Both compounds increased the rheobase current needed to trigger the first action potential, with **AT-17** requiring a higher threshold intensity than **AT**, suggesting a stronger inhibition of DRG neuron excitability (Fig. 5H). Both drugs also reduced the number of action potentials to double the rheobase current, with **AT-17** showing a more pronounced reduction in action potential amplitude, indicating its superior inhibitory effect (Fig. 5I and J). The current-voltage (I−V) relationship confirmed a significant shift for **AT-17**, with a 36.35% reduction in the peak current compared to **AT** (Fig. 5C). In TG neurons, neither **AT-17** nor **AT** affected the RMP, reinforcing their specificity for sodium channels. **AT-17** caused a notable increase in rheobase currents and reduced the number of action potentials more effectively than **AT**, demonstrating its potential to lower TG neuronal excitability (Fig. S2D and S2E). The amplitude of evoked action potentials was significantly attenuated by both compounds, with the I−V relationship showing a 10.56% reduction in peak current for **AT-17** compared to **AT**, suggesting a heightened inhibitory effect on sodium currents in TG neurons (Fig. S2F and S2C). These findings indicate that **AT-17** effectively inhibits sodium currents in both DRG and TG neurons, contributing to its higher anesthetic efficacy.

2.7. *Molecular dynamics simulation*

To further evaluate the differences between **AT** and **AT-17** when binding with $Na_V1.7$ and $Na_V1.8$, we conducted a 200 ns molecular dynamics simulation analysis. Stability was assessed using Root Mean Square Deviations (RMSDs), with the systems stabilizing after approximately 100 ns (Supporting Information Fig. S3A−S3D). In the $Na_V1.8$ complex, $Na_V1.8$-**AT-17** showed a notably lower RMSD than $Na_V1.8$-**AT**, indicating higher stability, whereas the differences between **AT** and **AT-17** in $Na_V1.7$ were minimal. The ligand RMSD values of the respective systems were similar. Root Mean Square Fluctuation (RMSF) and Radius of Gyration (Rg) analyses revealed conformational changes in the ion channel transmembrane domain, particularly a distinct rotational expansion in $Na_V1.8$-**AT-17** (Fig. S3E−S3H). In both the $Na_V1.7$ and $Na_V1.8$ complexes, RMSF changes were similar for **AT** and **AT-17**, suggesting sequence conservation. However, only in $Na_V1.8$-**AT-17** we observed significant rotational expansion. Binding mode analysis (Fig. 6A−D) showed that **AT** and **AT-17** obstructed ion penetration into the central cavity, with **AT-17** causing greater steric hindrance. **AT** forms hydrogen bonds and π−sulfur interactions, whereas **AT-17** establishes a hydrophobic barrier with the surrounding amino acids. Binding free energy calculations favored **AT-17** over **AT** with $Na_V1.7$ and $Na_V1.8$, showing a three-fold difference from $Na_V1.7$ (Table 4). Although **AT-17** increased the steric hindrance and polar solvation energy, its strong hydrophobic interactions, driven by van der Waals forces, provided greater stability in the binding cavity. Amino acid residue energy decomposition analysis revealed the distinct contributions of **AT** and **AT-17** to the binding of key residues (Supporting Information Fig. S4I and S4G). These computational findings support our earlier experimental results, confirming the superior inhibition of **AT-17** by $Na_V1.7$ and $Na_V1.8$ compared to **AT**.

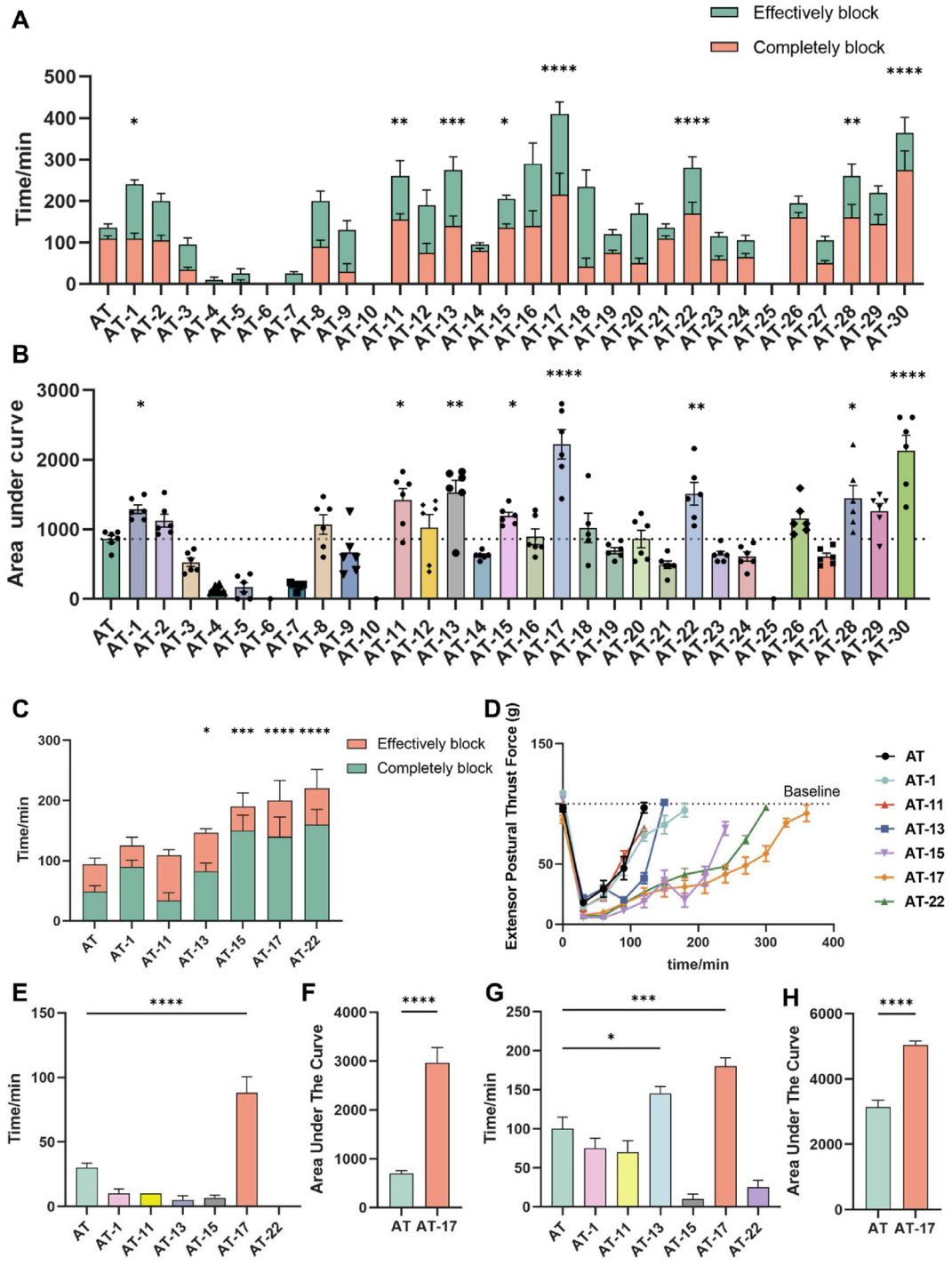

Figure 3 The evaluation of local anesthesia effects *in vivo*. (A) Duration of effectively block (≥50 % maximum possible effect, MPE) and completely block (100 % MPE) in cutaneous trunci pinprick model. The block duration of every compound compared with **AT**. (B) Statistics of the area under the curve of MPE. (C) Duration of effectively block and completely block in sensory evaluation of sciatic nerve block model; (D) Extensor postural thrust force in motor evaluation of sciatic nerve block model; (E, F) Chronic plantar inflammatory pain model induced by CFA, (E) duration of anesthesia in CFA-induced chronic inflammation model, (F) statistics of the area under the curve of (E); (G, H) Plantar incisional pain model, (G) duration of anesthesia in the plantar incisional pain model, (H) Statistics of the area under the curve of (G). Data were expressed as mean ± SEM, $n = 6$; *$P < 0.05$, **$P < 0.01$, ***$P < 0.001$ and ****$P < 0.0001$, *vs.* AT group.

2.8. *Anti-inflammation effect of* ***AT-17***

We further investigated the anti-inflammatory activity of **AT-17** and compared it with commonly used local anesthetics. After treating with lipopolysaccharide (LPS) for 24 h in DRG neurons and PC12 cells, we found **AT-17** significantly inhibited inflammatory factors (IL-1β, IL-6, TNFα), which was similar to LD and stronger than **AT** (Fig. 7A, Fig. S4A). We also examined the **AT-**

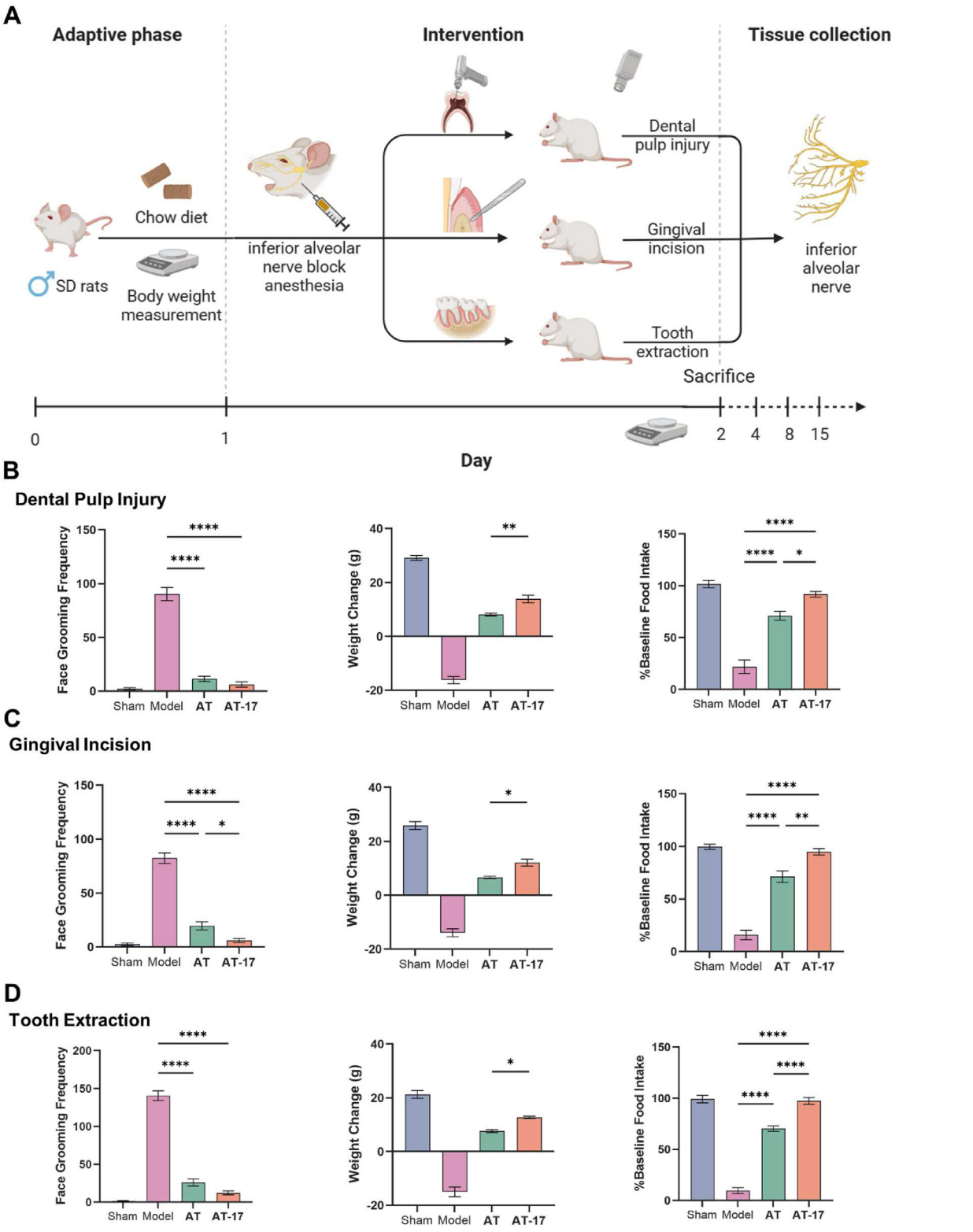

Figure 4 Comparation of **AT** and **AT-17** in oral pain models; (A) Establish evaluation procedure of oral animal pain model; (B) Effects of **AT** and **AT-17** on face grooming frequency (left), body weight (middle) and food intake (right) in dental pulp injury pain model; (C) Effects of **AT** and **AT-17** on face grooming frequency, body weight and food intake in gingival incision pain model; (D) Effects of **AT** and **AT-17** on face grooming frequency, body weight and food intake in tooth extraction pain model. Data are mean ± SEM, $n = 6$; $^{*}P < 0.05$, $^{**}P < 0.01$ and $^{****}P < 0.0001$.

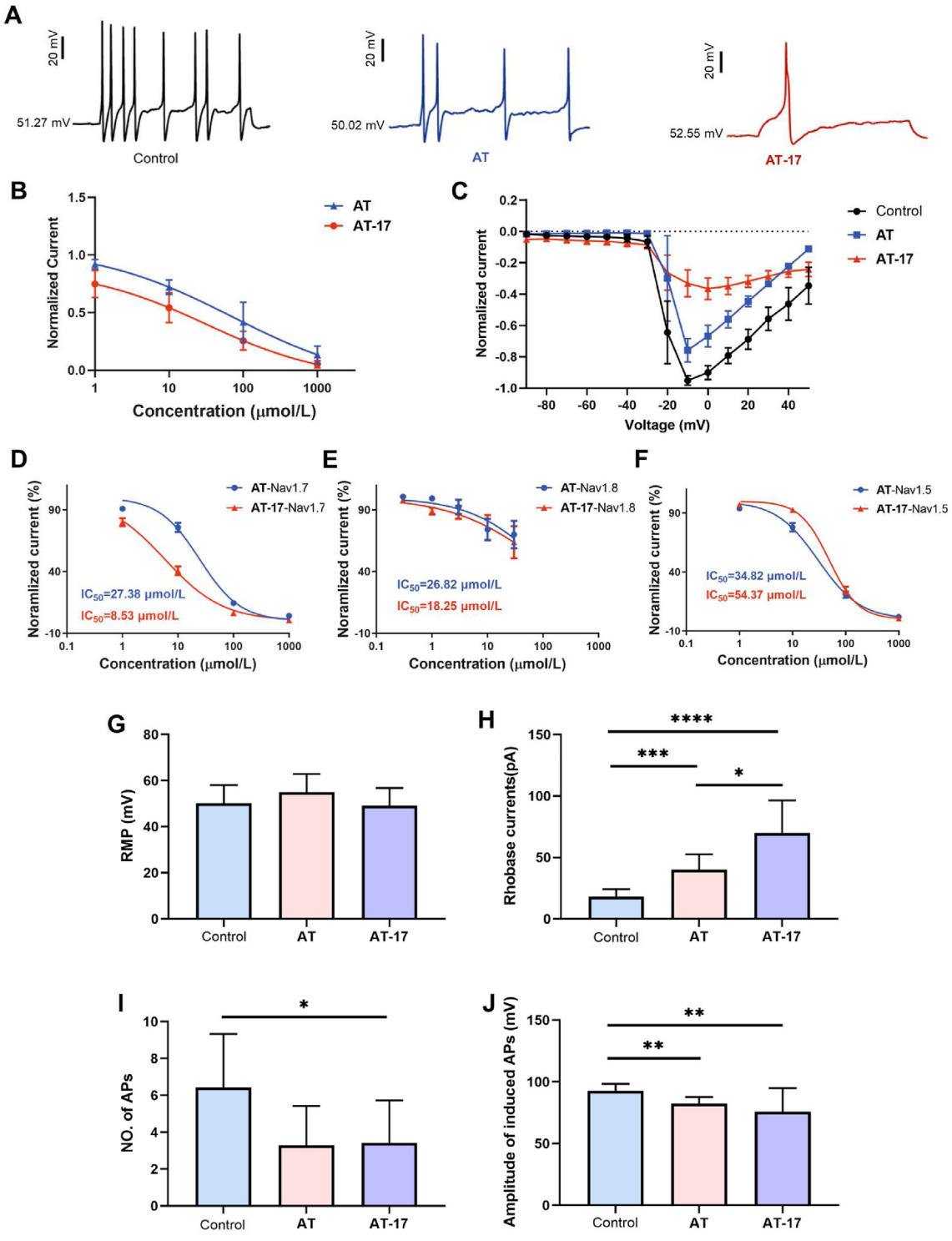

Figure 5 Electrophysiological effects of **AT** and **AT-17** on sodium ion channels. (A) Inhibitory effects of **AT** and **AT-17** on sodium current in rat DRG neurons; (B) Dose-dependent reduction in the peak current amplitude of **AT** and **AT-17** in rat DRG neurons; (C) the I−V relationship of **AT** and **AT-17** in rat DRG neurons; (D) Inhibition of sodium current by **AT** and **AT-17** in $Na_V1.7$-HEK293T cells; (E) Inhibition of sodium current by **AT** and **AT-17** in $Na_V1.8$-HEK293T cells; (F) Inhibition of sodium current by **AT** and **AT-17** in $Na_V1.5$-HEK293T cells; (G) Effect of **AT** and **AT-17** on resting membrane potential; (H) Effect of **AT** and **AT-17** in the rheobase current (I); Effect of **AT** and **AT-17** on the number of action potentials at twice the rheobase current; (J) Effect of **AT** and **AT-17** on the amplitude of evoked action potentials. Data are mean ± SEM. $n = 6$; $^*P < 0.05$, $^{**}P < 0.01$, $^{***}P < 0.001$ and $^{****}P < 0.0001$.

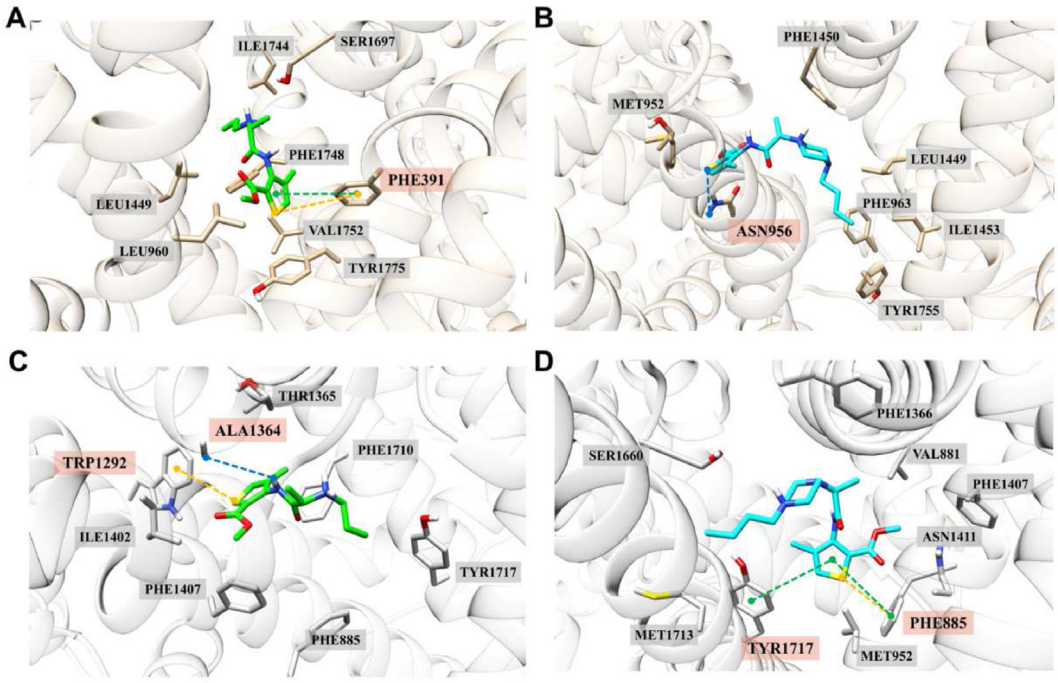

Figure 6 Molecular dynamics simulation between **AT/AT-17** and $Na_V1.7/1.8$ (A−D). Binding mode of the **AT** with $Na_V1.7$ (A), **AT-17** with $Na_V1.7$ (B), **AT** with $Na_V1.8$ (C), **AT-17** with $Na_V1.8$ (D). The dashed blue lines represent hydrogen bonds, the green lines represent $\pi-\pi$ interactions and the yellow lines represent $\pi-$sulfur interactions. Amino acid residues with key interactions are highlighted with a red background.

17 effect on both chronic (LPS treatment followed by **AT-17**, LPS (pre)) and acute (simultaneous LPS and **AT-17** treatment for 24 h, LPS (co)) inflammation models and observed substantial inhibition of inflammatory factor expression in nerve cells, more so than in immune cells (RAW 264.7 cells), as confirmed by ELISA results (Fig. S4C−S4E).

As IL-1β production is mainly regulated post-translationally, we examined the effects of **AT-17** on NLRP3 inflammasome activation. Regarding IL-1β production and NLRP3 inflammasome activation, **AT-17** modestly reduced NLRP3, ASC, and pro-Casp1 expression in both acute and chronic conditions and decreased Casp1 p20 secretion, with lesser effects in RAW 264.7 cells (Fig. 7B, Fig. S4B). **AT-17** also inhibits LPS-induced ASC speck formation, indicating a reduction in inflammasome assembly (Fig. 7C, Supporting Information Fig. S5A). What's more, another important function of NLRP3 and caspase 1 is to lyse GSDMD protein to form the active N-terminal and C-terminal, and GSDMD-N mediates cell membrane lysis and pyroptosis[42,43]. Thus, we examined whether pyroptosis occurred in nerve cells after LPS stimulation and whether our new drug could inhibit this pyroptosis. We found that LPS lysed GSDMD protein and increased the expression of N-terminal GSDMD protein, while **AT-17** could improve the increased N-terminal GSDMD expression (Supporting Information Fig. S11). Thus, we suggested that **AT-17** could improve LPS-induced pyroptosis. We further explored the mechanism of action of **AT-17** on NLRP3 inflammasome by focusing on oxidized mitochondrial DNA (oxmtDNA), which activates NLRP3. **AT-17** reduced LPS-induced ROS production, cytoplasmic mtDNA release, and 8-hydroxydeoxyguanosine (8-OHdG) levels, which are markers of oxidative stress (Fig. 7D−F, Fig. S5B−S5D). This effect was partially reversed by *tert*-butyl hydroperoxide (*t*-BHP, a ROS activator) and enhanced by mito-TEMPO (a mtROS scavenger) (Fig. 7G, Fig. S5E). *t*-BHP and mito-TEMPO also influence NLRP3 inflammasome activation, reversing or enhancing **AT-17** respectively (Fig. 7H, Supporting Information Figs. S5F−S5G, S6, S8, S9). Lastly, we investigated the effect of **AT-17** on IL-6 and TNFα, exploring the NF-κB, MAPK, and JNK pathways[44,45]. Using pathway activators (Betulinic acid for the NF-κB pathway, Skatole for the MAPK pathway and Anisomycin for JNK pathways), we found the MAPK pathway played a significant role in **AT-17** inhibitory effect on LPS-induced IL-6 and TNFα expressions in nerve cells (Supporting Information Fig. S7). In conclusion, **AT-17** reduced inflammation by decreasing mitochondrial ROS production and inhibiting NLRP3 inflammasome assembly.

2.9. *In vivo toxicity assessment*

In our safety evaluation, we initially assessed the systemic toxicity of **AT-17** by intravenous and subcutaneous administration. When

Table 4 Binding free energy of **AT** and **AT-17** binding with $Na_V1.7$ and $Na_V1.8$ (kcal/mol).

	Compd.	Coul energy	van der Waals energy	Polar solvation energy	SASA energy	ΔG_{bind}
$Na_V1.7$	**AT**	32.362	−116.651	59.490	−21.126	−5.388
	AT-17	−64.874	−171.107	150.068	−28.221	−17.346
$Na_V1.8$	**AT**	−60.771	−134.140	108.851	−22.588	−17.794
	AT-17	−59.956	−147.723	120.305	−27.725	−23.380

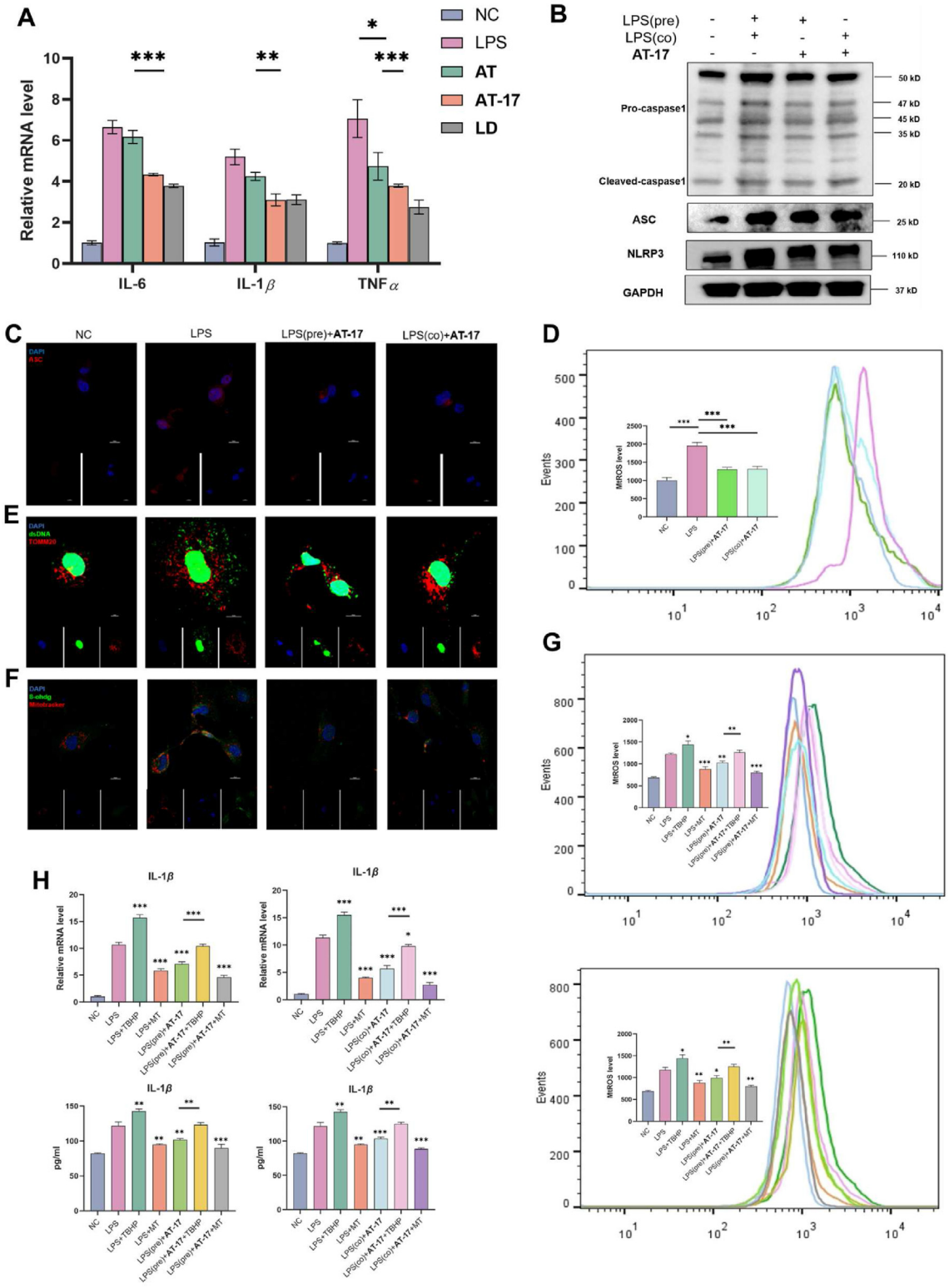

Figure 7 Anti-inflammatory effects of **AT-17** in DRG neurons. (A) RT-qPCR investigated the role of **AT**, **AT-17** and LD on the expressions of IL-1β, IL-6, and TNFα with LPS treatment. (B) The role of **AT-17** on the expressions of NLRP3, ASC and pro-Casp1 in DRG neurons. (C) The role of **AT-17** on the formation of ASC speck in DRG neurons. (D) The role of **AT-17** on the production of ROS in DRG neurons. (E) The role of **AT-17** on the cytoplasmic release of mtDNA in DRG neurons. (F) The role of **AT-17** on the level 8-ohdg in DRG neurons. (G) The role of t-BHP and mito-TEMPO on the function of **AT-17** on the production of LPS-caused ROS in both chronic (top) and acute (bottom) inflammation conditions. (H) The role of t-BHP and mito-TEMPO on the function of **AT-17** on the IL-1β expressions in chronic (left) and acute (right) inflammation conditions. Data are mean $\pm$ SEM; $^{*}P < 0.05$, $^{**}P < 0.01$ and $^{***}P < 0.001$. Scale bar $=$ 10 μm.

Table 5 Toxicological evaluation of AT and **AT-17.**

Compd.	LD_{50} (mg/kg)		ED_{50} (mg/kg)	TI[a]
	i.v.	s.c.	s.c.	
AT	38.32	597.72	4.75	125.83
AT-17	43.53	423.64	2.84	149.17

[a]TI = LD_{50}/ED_{50}.

administered intravenously *via* the tail vein (i.v.) in ICR mice, **AT-17** showed a median lethal dose (LD_{50}) of 43.53 mg/kg, indicating a more favorable safety profile than **AT** in this model. For subcutaneous injections (s.c.) in SD rats, The LD_{50} of **AT-17** was 423.64 mg/kg (Table 5), whereas **AT** was higher at 597.72 mg/kg. The median effective dose (ED_{50}) for s.c. was 4.75 mg/kg for **AT** and 2.84 mg/kg for **AT-17**. Consequently, the therapeutic index (TI) of **AT-17** is higher. Biochemical analyses of blood samples obtained from rats 7 days and 14 days post-administration evidenced no marked differences in ALT, AST, LDH, α-HBDH, CREA, or UREA levels between the control group and **AT-17** (Fig. 8B).

Local anesthetic toxicity in the nerves and organs was assessed, local reactions post-injection were not observed. Histopathological analysis of the sciatic and inferior alveolar nerves, as

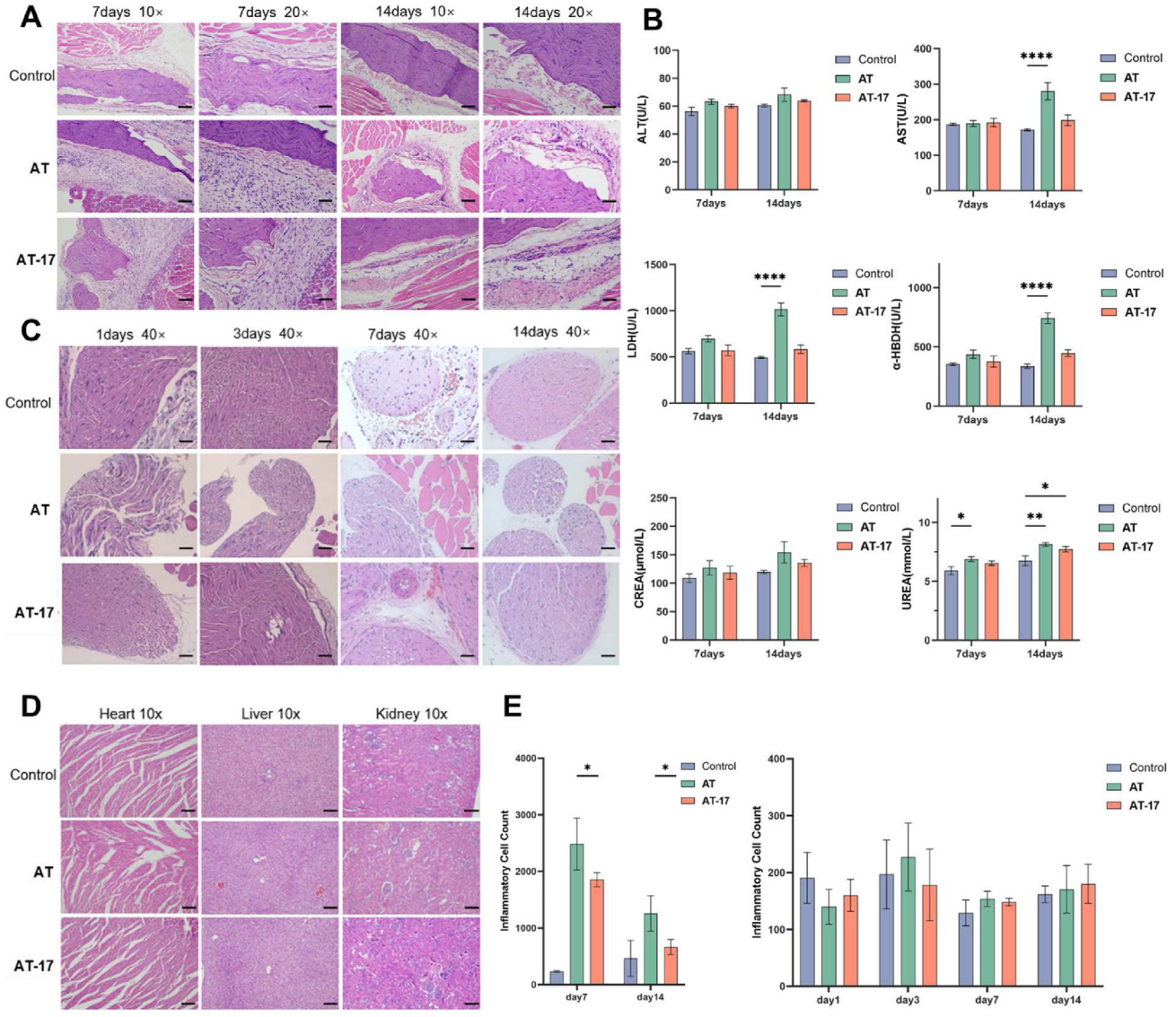

Figure 8 Toxicity of **AT-17**. (A) Hematoxylin-eosin (HE) pathological images of nerve and surrounding tissue after administration of sciatic nerve block model; (B) After administration, the blood biochemical indexes including AST, ALT, LDH, α-HBDH, CREA, UREA of **AT** group and **AT-17** group. (C) HE results of inferior alveolar nerve and surrounding tissue; (D) HE pathological images of important organs of rats after administration showed no obvious organic changes; (E) Computer software is used to count the number of inflammatory cells in sciatic nerve (20 ×) and inferior alveolar nerve (40 ×). Data are mean ± SEM; $n = 6$; *$P < 0.05$, **$P < 0.01$ and ****$P < 0.0001$. Scale bar = 100 μm (10 ×), 50 μm (20 ×), 25 μm (40 ×).

well as adjacent tissues, showed no evidence of necrosis (Fig. 8A−C). Quantitative analysis using ImageJ software demonstrated that the number of inflammatory cells in tissues treated with **AT-17** was significantly lower than that in tissues treated with **AT**. Notably, the inflammatory cell density in the inferior alveolar nerve was similar for both compounds (Fig. 8E).

To further substantiate these findings, we conducted pathological assessments of the heart, liver, and kidney following local **AT-17** administration to the sciatic nerve post-injection and found no significant pathological changes compared with the control group (Fig. 8D). We evaluated its effect on the hERG channel, a common toxicological target of various substances[46]. We measured the inhibition of the hERG potassium current by **AT-17** with an average inhibition rate of 37.985%, potentially contributing to its lower toxicity (Fig. S9). In summary, the results indicated a higher systemic and local safety profile of **AT-17**.

2.10. *Pharmacokinetic properties of* ***AT-17***

To investigate the pharmacokinetic parameters of **AT-17**, liver microsomes were first co-incubated with **AT-17** *in vitro*, revealing a time-dependent decrease in **AT-17** levels across various species (Supporting Information Fig. S12A). Additionally, the metabolic rate of **AT-17** in rat liver microsomes ($t_{1/2}$ = 1.032 h) closely resembled that in human liver microsomes ($t_{1/2}$ = 1.247 h, Fig. S12B). Given that the animal models used in this study were all rats, subsequent measurements were carried out to assess changes in blood concentrations following subcutaneous injection of **AT-17** in rats. The $t_{1/2}$ of **AT-17** is 0.823 h, the time to reach the maximum concentration (T_{max}) is 1.00 h, and the area under the plasma concentration-time curve (AUC_{0-t}) is 5549 h·ng/mL (Supporting Information Table S2). These findings indicate that **AT-17** can be metabolically stable in rats, does not exhibit accumulation, and probably possesses potential pharmacokinetic properties.

3. Conclusions

Multifunctional drugs have been proven effective in addressing the limitations of drugs with single or insufficient therapeutic effects. However, the integration of different pharmacophores within a confined single-molecule scaffold is challenging. In this study, we propose DeepSA, a novel deep-simulated annealing framework, to generate molecules for the development of multifunctional drugs. DeepSA integrates deep neural networks into metaheuristics (*i.e.*, simulated annealing) to restrict molecular space and improve exploration efficiency. We used DeepSA to generate articaine derivatives with anesthetic and anti-inflammatory effects. Based on the pool of generated derivatives, **AT-17** was through diverse validations *in vivo*. In electrophysiological experiments, we found that this compound had more advantages than articaine in inhibiting sodium ion channels and could selectively inhibit $Na_V1.7$ and $Na_V1.8$. In an investigation of the anti-inflammatory mechanism, this compound showed different functions in inhibiting the release of inflammatory cytokines in nerve cells compared to other local anesthetic drugs. Collectively, we developed an edit-based generative framework named DeepSA that utilizes deep simulated annealing to augment the ideal property by screening, which can be used to develop multifunctional drugs in the future. **AT-17** discovered based on this strategy can serve as a novel lead compound for local dental anesthetics that warrants further studies.

Despite the advantages of our method, this study has several limitations. Firstly, since DeepSA is a metaheuristic search algorithm toward an objective function, the generation quality of the DeepSA framework depends on the precise approximation of the objective. Secondly, the performance of DeepSA is sensitive to the initial molecules from where DeepSA starts. If the initial molecules are far from the optimal one (*i.e.*, with a high-scored objective value), the editing process would be complicated, hindering the generation of the desired molecules. In the future, we will explore causal learning techniques to enhance the planning ability of DeepSA.

4. Experimental

4.1. *Implementation details of DeepSA*

The hyperparameters utilized in the DeepSA model are as follows: T_{init} = 1.0, the decreasing rate C is set at 0.005, and the number of iterations for a search process N is specified as 50. The anti-inflammatory predictor was a three-layer message-passing neural network with hidden size of 300 and achieved convergence after 43 training epochs, yielding an overall test RMSE of 0.87 and a Pearson's correlation coefficient of 0.82. Regarding the editing operations, "replacement" involves substituting the atom at position k, "insertion" encompasses the addition of new atoms and corresponding chemical bonds to the original molecule, "deletion" entails the removal of the atom at position k and its attached chemical bonds, and "cyclization" denotes connecting two atoms to form a ring structure. In our pursuit of discovering novel dental anesthetics with more complex structures than articaine, our focus is on specific operations. Notably, the selection of operations is guided by varying probabilities: replacement: insertion: deletion: cyclization = 0.2: 0.5: 0.1: 0.2. Specifically, for our objectives, the higher probabilities assigned to "insertion" and "cyclization" align with the desired emphasis on adding complexity through the creation of new atoms and ring structures.

4.2. *Virtual screening based on deep learning models*

The active bases of the 433 generated molecules were subsequently initially verified by molecular docking in Discovery Studio 2019 (Accelrys, San Diego, CA, USA). The structures of $Na_V1.7$ complexed with IN2 (PDB ID: 7xmf[47], resolution: 3.07) and $Na_V1.8$ complexed with Amury803467 (PDB ID: 7we4[48], resolution: 2.70) were obtained from the Protein Data Bank. The binding site for local anesthetics in $Na_V1.7$ and $Na_V1.8$ was found to be located within the inner lumen of the channel pore and defined the circular docking box using Define Site. The 433 candidate molecules were converted into minimized 3D structures using the Ligand Preparation tool implemented. CDOCKER algorithm was used to perform docking minimization of the ligands into the defined binding site. The retrieved docked poses were submitted to in situ ligand minimization within the binding pocket to calculate the binding energy and complex energy of each pose. The results were visualized and analyzed using tools implemented in Discovery Studio 2019.

4.3. *Chemistry*

All starting materials and reagents were commercially available and used without further purification. All reactions were monitored by thin-layer chromatography (TLC) on a silica gel GF254 (0.25 mm, Qingdao Ocean Chemical, Ltd., China). Column chromatography (CC) was performed on a silica gel (200−300 mesh, Qingdao Ocean Chemical, Ltd., China). ^1H and ^{13}C NMR

spectra were recorded with a Bruker 400 MHz/100 MHz NMR spectrometer (Bruker, German) and referenced to deuterium oxide (D_2O), deuterated methanol (CD_3OD) or deuterated chloroform ($CDCl_3$). Chemical shifts are expressed in ppm. In the NMR tabulation, s indicates singlet; d, doublet; t, triplet; q, quartet; and m, multiplet. High-performance liquid chromatography (HPLC) analyses were performed on a Shimadzu HPLC system (Shimadzu, Japan) operating in a reverse mode with an MLtimate XB-C18 column (4.6 mm × 250 mm, 5 μm) using a water/methanol (each with 0.1% (*v/v*) trifluoroacetic acid) gradient at a flow rate at 1.0 mL/min. The purities of all final compounds were determined to be ≥ 95% by HPLC.

4.3.1. General procedure for the preparation of intermediates **2a–2c**

Methyl 3-amino-4-methylthiophene-2-carboxylate (1.0 eq.) and K_2CO_3 (2.0 eq.) were added to DCM and acyl bromide (1.3 eq.) diluted with DCM was dropped at −20 °C. The mixture was stirred for 24 h at room temperature. After being washed with water three times and dried by anhydrous Na_2SO_4, the solution was concentrated and PE was added. After sitting overnight and filtered, the target product was given.

*Methyl 3-(2-bromopropanamido)-4-methylthiophene-2-carboxylate (**2a**).* Yield: 97.8%, off-white solid. ^{1}H NMR (400 MHz, $CDCl_3$) δ 9.28 (s, 1H), 7.14 (s, 1H), 4.55 (q, J = 7.0 Hz, 1H), 3.86 (s, 3H), 2.16 (s, 3H), 1.95 (d, J = 7.0 Hz, 3H).

*Methyl 3-(2-bromoacetamido)-4-methylthiophene-2-carboxylate (**2b**).* Yield: 88.8%, white solid. ^{1}H NMR (400 MHz, $CDCl_3$) δ 9.42 (s, 1H), 7.17 (s, 1H), 4.04 (s, 2H), 3.88 (s, 3H), 2.19 (d, J = 1.0 Hz, 3H).

*Methyl 3-(2-bromobutanamido)-4-methylthiophene-2-carboxylate (**2c**).* Yield: 87.0%, white solid. ^{1}H NMR (400 MHz, $CDCl_3$) δ 9.32 (s, 1H), 7.16 (s, 1H), 4.39 (dd, J = 7.8, 5.7 Hz, 1H), 3.88 (s, 3H), 2.32−2.08 (m, 5H), 1.13 (t, J = 7.3 Hz, 3H).

4.3.2. General procedure for the preparation of intermediates **4a–4e**

To a solution of *tert*-butyl 1-piperazinecarboxylate (1.0 eq.) and K_2CO_3 (2.0 eq.) in CH_3CN, the bromide (1.2 eq.) was added into the mixture. The mixture was stirred at room temperature overnight. After filtered, the mixture was concentrated under reduced pressure and purified by chromatography (PE/EA = 4:1). Then, TFA/DCM (1:1) was added, and the reaction mixture was stirred at room temperature for 1 h. The solution was concentrated to give the target product without further purification.

*1-(Cyclopropylmethyl)piperazine (**4a**).* Yield: 96.9%, colorless oil. ^{1}H NMR (400 MHz, CD_3OD) δ 3.83−3.52 (m, 8H), 3.17 (d, J = 7.4 Hz, 2H), 1.20−1.08 (m, 1H), 0.82−0.76 (m, 2H), 0.46 (dt, J = 6.2, 4.7 Hz, 2H).

*1-Propylpiperazine (**4b**).* Yield: 74.6%, colorless oil. ^{1}H NMR (400 MHz, CD_3OD) δ 3.62−3.38 (m, 8H), 3.15−3.06 (m, 2H), 1.83−1.69 (m, 2H), 1.02 (t, J = 7.4 Hz, 3H).

*1-Butylpiperazine (**4c**).* Yield: 74.2%, colorless oil. ^{1}H NMR (400 MHz, CD_3OD) δ 3.57 (s, 8H), 3.25−3.17 (m, 2H), 1.79−1.68 (m, 2H), 1.49−1.37 (m, 2H), 1.00 (t, J = 7.4 Hz, 3H).

*2-(Piperazin-1-yl)ethan-1-ol (**4d**).* Yield: 26.7%, colorless oil. ^{1}H NMR (400 MHz, CD_3OD) δ 3.90−3.82 (m, 2H), 3.55−3.40 (m, 8H), 3.23−3.16 (m, 2H).

*1-(2-Methoxyethyl)piperazine (**4e**).* Yield: 53.0%, colorless oil. ^{1}H NMR (400 MHz, D_2O) δ 3.68−3.62 (m, 2H), 3.47 (s, 8H), 3.33−3.29 (m, 2H), 3.25 (s, 3H).

4.3.3. Synthetic sequence for tert-butyl 4-(1-((2-(methoxycarbonyl)-4-methylthiophen-3-yl)amino)-1-oxopropan-2-yl)piperazine-1-carboxylate (intermediate **AT-1-Boc**)

To a solution of compound **2a** (2.0 g, 6.53 mmol) and K_2CO_3 (1.81 g, 13.06 mmol) in 30 mL DMF/CH_3CN (1:1), *tert*-butyl piperazine-1-carboxylate (1.46 g, 7.84 mmol) was added into the mixture. The mixture was stirred at room temperature for 9 h. The mixture was concentrated, diluted with 100 mL DCM, washed with 100 mL water four times, dried over Na_2SO_4, filtered, and concentrated. The residue was purified by chromatography (DCM/MeOH = 50:1) to yield **AT-1-Boc** (2.68 g, 99.7%) as a colorless oil. ^{1}H NMR (400 MHz, $CDCl_3$) δ 10.03 (s, 1H), 7.12 (s, 1H), 3.83 (s, 3H), 3.66−3.52 (m, 4H), 3.23 (q, J = 7.0 Hz, 1H), 2.71−2.46 (m, 4H), 2.17 (d, J = 1.0 Hz, 3H), 1.47 (s, 9H), 1.33 (d, J = 7.0 Hz, 3H).

4.3.4. Synthetic sequence for methyl 4-methyl-3-(2-(piperazin-1-yl)propanamido)thiophene-2-carboxylate (final compounds **AT-1**)

To a solution of compound **AT-1-Boc** (2.68 g, 6.51 mmol) in 10 mL 1,4-dioxane, hydrogen chloride 1,4-dioxane (4 mol/L; 4 mL, 16 mmol) was added. The mixture was stirred at room temperature for 5 h and gave a white precipitate. After filtered, the residue was washed by 1,4-dioxane to afford **AT-1** (2.0 g, 79.8%) as a white oil. ^{1}H NMR (400 MHz, D_2O) δ 7.47 (d, J = 10.8 Hz, 1H), 4.52−4.33 (m, 1H), 3.92−3.79 (m, 5H), 3.78−3.65 (m, 6H), 2.18−2.02 (m, 3H), 1.80 (d, J = 7.0 Hz, 3H). ^{13}C NMR (101 MHz, D_2O) δ 168.20, 163.08, 163.04, 136.64, 136.61, 128.43, 124.49, 124.44, 64.24, 52.52, 46.97, 40.89, 40.86, 13.95, 13.91, 12.84, 12.80. HRMS (ESI) *m/z*: calcd for $C_{14}H_{22}N_3O_3S$, 312.1376; found 312.1367 $[M + H]^+$. HPLC purity: 99.543%, t_R = 17.497 min.

4.3.5. General procedure for the preparation of final compounds **AT-2–13**, **15**, **21–26**

To a solution of intermediates **2a–2c** (1.0 eq.) and K_2CO_3 (2.0 eq.) in DMF, the amines (1.2 eq.) were added into the mixture, and the reaction was stirred at 50 °C for 3−5 h. After the solution was cooled, diluted DCM, washed with water four times, dried over anhydrous Na_2SO_4, filtered, and concentrated. The residue was purified by chromatography (DCM/MeOH = 40:1) to yield the target product. Hydrochloric acid solution (2 mol/L) was added to a solution of the target product in MeOH, and the reaction was stirred at room temperature for 1 h. After concentrated under reduced pressure, the residue was dissolved in water, filtered, and freeze dried to give hydrochloride compound.

*Methyl 3-(2-(3,4-dimethylpiperazin-1-yl)propanamido)-4-methylthiophene-2-carboxylate (**AT-2**).* Yield: 52.3%, pale-yellow oil. ^{1}H NMR (400 MHz, $CDCl_3$) δ 9.87 (d, J = 18.2 Hz, 1H), 7.10 (s, 1H), 3.82 (s, 3H), 3.26−3.08 (m, 1H), 2.92−2.73 (m, 3H), 2.65−2.41 (m, 2H), 2.31 (s, 3H), 2.26−2.02 (m, 5H), 1.32 (dd, J = 7.0, 2.5 Hz, 3H), 1.07 (dd, J = 8.7, 6.2 Hz, 3H). ^{13}C NMR (101 MHz, $CDCl_3$) δ 172.61, 172.45, 162.74, 141.86, 141.80, 136.25, 127.00, 118.52, 118.43, 64.75, 64.68, 59.98, 58.02, 57.93, 55.85, 54.83, 52.68, 51.74, 47.88, 42.45, 42.41, 15.54, 15.48, 12.72, 12.10. HRMS (ESI) *m/z*: calcd for $C_{16}H_{26}N_3O_3S$, 340.1689; found 340.1679 $[M + H]^+$. HPLC purity: 99.293%, t_R = 18.441 min.

*Methyl 4-methyl-3-(2-(piperidin-1-yl)propanamido)thiophene-2-carboxylate (**AT-3**).* Yield: 74.0%, 74.0%. Pale-yellow solid, m.p. 63−64 °C. ^{1}H NMR (400 MHz, $CDCl_3$) δ 10.01 (s, 1H), 7.10 (s, 1H), 3.83 (s, 3H), 3.20 (q, J = 7.0 Hz, 1H), 2.76−2.41 (m, 4H), 2.16 (d, J = 1.0 Hz, 3H), 1.77−1.62 (m, 4H), 1.54−1.42

(m, 2H), 1.31 (d, J = 7.0 Hz, 3H). ^{13}C NMR (101 MHz, $CDCl_3$) δ 172.95, 162.71, 141.79, 136.20, 126.94, 118.55, 65.39, 51.78, 51.42, 26.24, 24.25, 15.57, 11.71. HRMS (ESI) *m/z*: calcd for $C_{15}H_{23}N_2O_3S$, 311.1424; found 311.1413 $[M + H]^+$. HPLC purity: 95.461%, t_R = 17.941 min.

*Methyl 3-(2-(3,5-dimethylpiperidin-1-yl)propanamido)-4-methylthiophene-2-carboxylate (**AT-4**)*. Yield: 80.8%, colorless oil. ^{1}H NMR (400 MHz, D_2O) δ 7.46 (s, 1H), 4.20 (q, J = 6.9 Hz, 1H), 3.83 (s, 3H), 3.67−3.55 (d, J = 11.5 Hz, 1H), 3.42 (d, J = 11.4 Hz, 1H), 2.75 (t, J = 12.0 Hz, 1H), 2.61 (t, J = 12.0 Hz, 1H), 2.08 (s, 3H), 2.04−1.84 (m, 3H), 1.74 (d, J = 7.0 Hz, 3H), 1.01−0.84 (m, 7H). ^{13}C NMR (151 MHz, D_2O) δ 168.75, 163.06, 136.69, 136.59, 128.34, 124.47, 64.17, 57.70, 55.18, 52.44, 38.27, 29.04, 28.70, 17.65, 17.58, 13.80, 12.74. HRMS (ESI) *m/z*: calcd for $C_{17}H_{27}N_2O_3S$, 339.1737; found 339.1732 $[M + H]^+$. HPLC purity: 96.029%, t_R = 19.084 min.

*Methyl 4-methyl-3-(2-morpholinopropanamido)thiophene-2-carboxylate (**AT-5**)*. Yield: 51.0%, colorless oil. ^{1}H NMR (400 MHz, $CDCl_3$) δ 10.00 (s, 1H), 7.18−7.02 (m, 1H), 3.91−3.77 (m, 7H), 3.16 (q, J = 7.0 Hz, 1H), 2.72−2.53 (m, 4H), 2.15 (d, J = 0.9 Hz, 3H), 1.34 (d, J = 7.0 Hz, 3H). ^{13}C NMR (101 MHz, $CDCl_3$) δ 172.31, 162.87, 141.96, 136.11, 127.25, 127.21, 118.00, 67.14, 65.39, 51.86, 51.79, 50.71, 15.68, 15.64, 12.74, 12.71. HRMS (ESI) *m/z*: calcd for $C_{14}H_{21}N_2O_4S$, 313.1217; found 313.1210 $[M + H]^+$. HPLC purity: 99.358%, t_R = 16.611 min.

*Methyl 4-methyl-3-(2-(3-methylmorpholino)propanamido)thiophene-2-carboxylate (**AT-6**)*. Yield: 21.0%, white oil. ^{1}H NMR (400 MHz, $CDCl_3$) δ 10.19 (s, 1H), 7.11 (s, 1H), 3.92−3.74 (m, 7H), 3.42 (dd, J = 10.8, 9.1 Hz, 1H), 2.85−2.76 (m, 1H), 2.68−2.55 (m, 2H), 2.16 (s, 3H), 1.26 (d, J = 7.0 Hz, 3H), 1.07 (d, J = 6.3 Hz, 3H). ^{13}C NMR (101 MHz, $CDCl_3$) δ 172.50, 162.81, 142.20, 136.06, 127.13, 117.76, 73.36, 67.36, 58.11, 52.22, 51.77, 46.64, 15.75, 14.23, 8.67. HRMS (ESI) *m/z*: calcd for $C_{15}H_{23}N_2O_4S$, 327.1373; found 327.1364 $[M + H]^+$. HPLC purity: 95.906%, t_R = 15.160 min and 16.403 min.

*Methyl 3-(2-(3,5-dimethylmorpholino)propanamido)-4-methylthiophene-2-carboxylate (**AT-7**)*. Yield: 77.1%, colorless oil. ^{1}H NMR (400 MHz, D_2O) δ 7.48 (s, 1H), 4.27 (q, J = 6.8 Hz, 1H), 4.15−3.98 (m, 2H), 3.84 (s, 3H), 3.68 (d, J = 12.2 Hz, 1H), 3.52 (d, J = 12.1 Hz, 1H), 3.02 (t, J = 11.6 Hz, 1H), 2.92 (t, J = 11.7 Hz, 1H), 2.09 (s, 3H), 1.76 (d, J = 6.9 Hz, 3H), 1.27 (dd, J = 14.0, 6.3 Hz, 6H). ^{13}C NMR (151 MHz, D_2O) δ 168.18, 163.02, 136.54, 136.52, 128.32, 124.49, 69.52, 64.51, 55.06, 52.85, 52.41, 17.40, 17.28, 13.68, 12.68. HRMS (ESI) *m/z*: calcd for $C_{16}H_{25}N_2O_4S$, 341.1530; found 341.1523 $[M + H]^+$. HPLC purity: 98.351%, t_R = 16.100 min.

*Methyl 4-methyl-3-(2-(2,2,6-trimethylmorpholino)propanamido)thiophene-2-carboxylate (**AT-8**)*. Yield: 61.7%, colorless oil. ^{1}H NMR (400 MHz, $CDCl_3$) δ 9.96 (d, J = 63.7 Hz, 1H), 7.12 (s, 1H), 4.23−4.12 (m, 1H), 3.82 (d, J = 1.8 Hz, 3H), 3.30−2.99 (m, 1H), 2.85−2.68 (m, 1H), 2.68−2.53 (m, 1H), 2.34 (d, J = 10.9 Hz, 1H), 2.17 (dd, J = 3.0, 0.8 Hz, 3H), 1.92 (q, J = 11.1 Hz, 1H), 1.44 (d, J = 8.9 Hz, 3H), 1.34 (d, J = 7.0 Hz, 1H), 1.28 (d, J = 7.0 Hz, 2H), 1.22 (d, J = 3.6 Hz, 3H), 1.15−1.08 (m, 3H). ^{13}C NMR (101 MHz, D_2O) δ 168.36, 167.97, 163.07, 136.79, 136.64, 136.52, 136.45, 128.38, 128.34, 124.39, 71.72, 71.62, 65.08, 64.36, 63.70, 59.03, 55.57, 54.70, 52.97, 52.48, 52.40, 27.36, 27.09, 20.65, 17.71, 13.75, 12.73, 12.01. HRMS (ESI) *m/z*: calcd for $C_{17}H_{27}N_2O_4S$, 355.1686; found 355.1680 $[M + H]^+$. HPLC purity: 96.215%, t_R = 19.348 min and 19.955 min.

*Methyl 4-methyl-3-(2-thiomorpholinopropanamido)thiophene-2-carboxylate (**AT-9**)*. Yield: 88.9%. Colorless solid, m.p. 99−100 °C. ^{1}H NMR (400 MHz, $CDCl_3$) δ 10.06 (s, 1H), 7.19−7.02 (m, 1H), 3.83 (s, 3H), 3.32 (q, J = 7.0 Hz, 1H), 3.02−2.91 (m, 2H), 2.84 (d, J = 6.4 Hz, 6H), 2.16 (d, J = 0.9 Hz, 3H), 1.31 (d, J = 7.0 Hz, 3H). ^{13}C NMR (151 MHz, D_2O) δ 168.22, 163.00, 136.61, 136.56, 128.32, 124.45, 64.02, 52.42, 24.19, 13.44, 12.71. HRMS (ESI) *m/z*: calcd for $C_{14}H_{21}N_2O_3S_2$, 329.0988; found 329.0980 $[M + H]^+$. HPLC purity: 96.255%, t_R = 16.582 min.

*Methyl 3-(2-(1,1-dioxidothiomorpholino)propanamido)-4-methylthiophene-2-carboxylate (**AT-10**)*. Yield: 31.9%, pale-yellow oil. ^{1}H NMR (400 MHz, $CDCl_3$) δ 10.10 (s, 1H), 7.13 (d, J = 1.2 Hz, 1H), 3.82 (s, 3H), 3.51 (q, J = 7.0 Hz, 1H), 3.38−3.04 (m, 8H), 2.16 (d, J = 1.0 Hz, 3H), 1.34 (d, J = 7.0 Hz, 3H). ^{13}C NMR (101 MHz, $CDCl_3$) δ 170.48, 163.40, 142.22, 135.87, 127.76, 117.27, 64.49, 52.02, 51.67, 48.49, 15.82, 10.85. HRMS (ESI) *m/z*: calcd for $C_{14}H_{21}N_2O_5S_2$, 361.0886; found 361.0879 $[M + H]^+$. HPLC purity: 98.852%, t_R = 20.326 min.

*Methyl 4-methyl-3-(2-(4-methylpiperazin-1-yl)propanamido)thiophene-2-carboxylate (**AT-11**)*. Yield: 61.7%. Colorless solid, m.p. 86−87 °C ^{1}H NMR (400 MHz, $CDCl_3$) δ 9.87 (s, 1H), 7.17−7.00 (m, 1H), 3.81 (s, 3H), 3.18 (q, J = 7.0 Hz, 1H), 2.77−2.46 (m, 7H), 2.36 (d, J = 8.6 Hz, 1H), 2.30 (s, 3H), 2.17−2.08 (m, 3H), 1.31 (d, J = 7.0 Hz, 3H). ^{13}C NMR (101 MHz, $CDCl_3$) δ 172.54, 162.72, 141.78, 136.20, 127.10, 127.02, 118.45, 64.84, 55.28, 51.86, 51.76, 46.10, 46.02, 15.60, 15.55, 12.59, 12.53. HRMS (ESI) *m/z*: calcd for $C_{15}H_{24}N_3O_3S$, 326.1533; found 326.1526 $[M + H]^+$. HPLC purity: 98.402%, t_R = 14.715 min.

*Methyl 3-(2-(4-ethylpiperazin-1-yl)propanamido)-4-methylthiophene-2-carboxylate (**AT-12**)*. Yield: 88.4%, yellow oil. ^{1}H NMR (400 MHz, $CDCl_3$) δ 9.90 (s, 1H), 7.11 (d, J = 0.9 Hz, 1H), 3.83 (s, 3H), 3.21 (q, J = 7.0 Hz, 1H), 2.98−2.48 (m, 8H), 2.45 (q, J = 7.2 Hz, 2H), 2.15 (d, J = 0.9 Hz, 3H), 1.34 (d, J = 7.0 Hz, 3H), 1.10 (t, J = 7.2 Hz, 3H). ^{13}C NMR (151 MHz, D_2O) δ 174.13, 163.21, 137.88, 136.70, 128.09, 123.71, 63.16, 52.31, 51.94, 50.87, 13.61, 12.94, 8.52. HRMS (ESI) *m/z*: calcd for $C_{16}H_{26}N_3O_3S$, 340.1689; found 340.1685 $[M + H]^+$. HPLC purity: 99.316%, t_R = 15.207 min.

*Methyl 3-(2-(4-isopropylpiperazin-1-yl)propanamido)-4-methylthiophene-2-carboxylate (**AT-13**)*. Yield: 97.8%, colorless oil. The preparation of hydrochloride compound was same as **AT**. ^{1}H NMR (400 MHz, $CDCl_3$) δ 9.93 (s, 1H), 7.19−7.01 (m, 1H), 3.83 (s, 3H), 3.20 (q, J = 7.0 Hz, 1H), 2.87−2.49 (m, 9H), 2.16 (d, J = 0.9 Hz, 3H), 1.34 (d, J = 7.0 Hz, 3H), 1.08 (d, J = 6.5 Hz, 6H). ^{13}C NMR (151 MHz, D_2O) δ 173.85, 163.22, 137.85, 136.69, 128.11, 123.71, 63.16, 58.43, 52.32, 47.62, 16.05, 13.64, 12.94. HRMS (ESI) *m/z*: calcd for $C_{17}H_{28}N_3O_3S$, 354.1846; found 354.1840 $[M + H]^+$. HPLC purity: 98.948%, t_R = 15.932 min.

*Methyl 3-(2-(4-(tert-butyl)piperazin-1-yl)propanamido)-4-methylthiophene-2-carboxylate (**AT-15**)*. Yield: 70.8%, white oil. ^{1}H NMR (400 MHz, $CDCl_3$) δ 9.91 (s, 1H), 7.10 (s, 1H), 3.81 (s, 3H), 3.17 (q, J = 7.0 Hz, 1H), 2.90−2.42 (m, 8H), 2.14 (d, J = 0.9 Hz, 3H), 1.32 (d, J = 7.0 Hz, 3H), 1.08 (s, 9H). ^{13}C NMR (101 MHz, $CDCl_3$) δ 172.76, 162.70, 141.80, 136.19, 127.11, 127.04, 118.49, 64.83, 53.74, 51.83, 51.72, 45.84, 25.92, 25.86, 15.63, 15.58, 15.54, 12.74, 12.67. HRMS (ESI) *m/z*: calcd for $C_{18}H_{30}N_3O_3S$, 368.2002; found 368.1995 $[M + H]^+$. HPLC purity: 98.050%, t_R = 15.109 min.

*Methyl 3-(2-(4-isopropylpiperazin-1-yl)acetamido)-4-methylthiophene-2-carboxylate (**AT-21**)*. Yield: 46.3%, colorless oil. ^{1}H NMR (400 MHz, $CDCl_3$) δ 9.91 (s, 1H), 7.12 (s, 1H), 3.83 (s, 3H), 3.18 (s, 2H), 2.84−2.56 (m, 9H), 2.18 (s, 3H), 1.08 (d, J = 6.5 Hz,

6H). ^{13}C NMR (101 MHz, $CDCl_3$) δ 167.83, 161.70, 140.49, 135.23, 126.11, 117.67, 61.03, 53.47, 52.97, 50.77, 47.70, 17.65, 14.59. HRMS (ESI) *m/z*: calcd for $C_{16}H_{26}N_3O_3S$, 340.1689; found 340.1679 $[M + H]^+$. HPLC purity: 97.830%, t_R = 17.898 min.

*Methyl 3-(2-(4-isopropylpiperazin-1-yl)butanamido)-4-methylthiophene-2-carboxylate (**AT-22**).* Yield: 28.7%, colorless oil. ^{1}H NMR (400 MHz, $CDCl_3$) δ 9.80 (s, 1H), 7.09 (d, J = 1.5 Hz, 1H), 3.81 (s, 3H), 2.94−2.88 (m, 1H), 2.82−2.54 (m, 9H), 2.17 (d, J = 1.4 Hz, 3H), 1.90−1.72 (m, 2H), 1.06 (d, J = 6.3 Hz, 6H), 1.02 (t, J = 7.4 Hz, 3H). ^{13}C NMR (101 MHz, $CDCl_3$) δ 170.73, 161.90, 141.18, 135.03, 126.24, 116.70, 70.52, 53.50, 50.74, 47.86, 20.80, 17.63, 17.59, 15.02, 10.19. HRMS (ESI) *m/z*: calcd for $C_{18}H_{30}N_3O_3S$, 368.2002; found 368.1990 $[M + H]^+$. HPLC purity: 99.081%, t_R = 19.175 min.

*Methyl 3-(2-(bis(2-methoxyethyl)amino)propanamido)-4-methylthiophene-2-carboxylate (**AT-23**).* Yield: 17.9%. Colorless solid, m.p. 110−111 °C. ^{1}H NMR (400 MHz, $CDCl_3$) δ 9.99 (s, 1H), 7.18−7.03 (m, 1H), 3.82 (s, 3H), 3.68 (q, J = 7.0 Hz, 1H), 3.60−3.49 (m, 4H), 3.31 (s, 6H), 2.91−2.71 (m, 4H), 2.18−2.11 (m, 3H), 1.32 (d, J = 7.0 Hz, 3H). ^{13}C NMR (101 MHz, $CDCl_3$) δ 172.82, 162.49, 141.58, 136.23, 126.73, 126.64, 119.42, 71.76, 61.58, 61.49, 58.84, 51.80, 51.68, 50.80, 15.35, 15.29, 10.17, 10.11. HRMS (ESI) *m/z*: calcd for $C_{16}H_{27}N_2O_5S$, 359.1635; found 359.1630 $[M + H]^+$. HPLC purity: 95.108%, t_R = 14.932 min.

*Methyl 3-(2-(ethyl(2-hydroxyethyl)amino)propanamido)-4-methylthiophene-2-carboxylate (**AT-24**).* Yield: 35.3%, colorless oil. ^{1}H NMR (400 MHz, $CDCl_3$) δ 10.48 (s, 1H), 7.13 (s, 1H), 3.83 (s, 3H), 3.79−3.62 (m, 2H), 3.57 (q, J = 7.0 Hz, 1H), 3.53−3.35 (m, 1H), 2.88−2.78 (m, 1H), 2.71−2.51 (m, 3H), 2.22 (s, 3H), 1.31 (d, J = 7.0 Hz, 3H), 1.13 (t, J = 7.1 Hz, 3H). ^{13}C NMR (101 MHz, $CDCl_3$) δ 172.70, 163.79, 143.16, 135.91, 127.95, 116.76, 60.60, 60.16, 53.07, 52.13, 44.81, 16.00, 13.39, 9.28. HRMS (ESI) *m/z*: calcd for $C_{14}H_{23}N_2O_4S$, 315.1373; found 315.1364 $[M + H]^+$. HPLC purity: 95.438%, t_R = 17.154 min.

*Methyl 3-(2-(bis(2-hydroxyethyl)amino)propanamido)-4-methylthiophene-2-carboxylate (**AT-25**).* Yield: 19.7%, grey oil. ^{1}H NMR (400 MHz, $CDCl_3$) δ 10.29 (s, 1H), 7.14 (d, J = 1.4 Hz, 1H), 3.82 (d, J = 1.6 Hz, 3H), 3.81−3.58 (m, 6H), 3.55 (q, J = 7.1 Hz, 1H), 2.85−2.76 (m, 2H), 2.66 (d, J = 13.8 Hz, 2H), 2.17 (s, 3H), 1.34 (dd, J = 7.1, 1.8 Hz, 3H). ^{13}C NMR (101 MHz, $CDCl_3$) δ 172.21, 163.91, 142.75, 136.47, 128.00, 118.01, 60.95, 60.17, 52.54, 52.24, 15.57, 9.40. HRMS (ESI) *m/z*: calcd for $C_{14}H_{23}N_2O_5S$, 331.1322; found 331.1313 $[M + H]^+$. HPLC purity: 99.487%, t_R = 16.202 min.

*Methyl 4-methyl-3-(2-((2-morpholinoethyl)amino)propanamido)thiophene-2-carboxylate (**AT-26**).* Yield: 94.8%, pale-yellow oil. ^{1}H NMR (400 MHz, $CDCl_3$) δ 10.04 (s, 1H), 7.12 (s, 1H), 3.82 (s, 3H), 3.68 (t, J = 4.5 Hz, 4H), 3.30 (q, J = 6.9 Hz, 1H), 2.90−2.70 (m, 2H), 2.66−2.35 (m, 6H), 2.16 (s, 3H), 1.41 (d, J = 6.9 Hz, 3H). ^{13}C NMR (101 MHz, $CDCl_3$) δ 173.85, 162.91, 141.94, 136.14, 127.25, 118.39, 67.02, 59.18, 58.09, 53.71, 53.47, 51.83, 44.94, 20.09, 15.53. HRMS (ESI) *m/z*: calcd for $C_{16}H_{26}N_3O_4S$, 356.1639; found 356.1630 $[M + H]^+$. HPLC purity: 99.524%, t_R = 13.584 min.

*4.3.6. General procedure for the preparation of final compounds **AT, AT-14, 16−20***

To a solution of compound **2a** (1.0 eq.) and K_2CO_3 (2.0 eq.) in 30 mL DMF, the amine (1.2 eq.) was dropped into the mixture, and the reaction was stirred at room temperature for 5−12 h. The mixture was diluted with DCM, washed with water four times, dried over anhydrous Na_2SO_4, and removed solvent under vacuum concentration to acquire the target product. Hydrochloric acid solution (2 mol/L) was added to a solution of the target product in MeOH, and the reaction was stirred at room temperature for 1 h. After concentrated under reduced pressure, the residue was dissolved in water, filtered, and freeze dried to give hydrochloride compound.

*Methyl 4-methyl-3-(2-(propylamino)propanamido)thiophene-2-carboxylate (**AT**).* Yield: 93.2%, pale-yellow oil. ^{1}H NMR (400 MHz, D_2O) δ 7.45 (s, 1H), 4.28 (q, J = 7.0 Hz, 1H), 3.82 (s, 3H), 3.18−2.91 (m, 2H), 2.07 (s, 3H), 1.80−1.72 (m, 2H), 1.70 (d, J = 6.8 Hz, 3H), 0.98 (t, J = 7.4 Hz, 3H).

*Methyl 3-(2-(4-(cyclopropylmethyl)piperazin-1-yl)propanamido)-4-methylthiophene-2-carboxylate (**AT-14**).* Yield: 82.0%, colorless oil. ^{1}H NMR (400 MHz, $CDCl_3$) δ 9.91 (s, 1H), 7.10 (s, 1H), 3.82 (s, 3H), 3.21 (q, J = 7.0 Hz, 1H), 2.96−2.38 (m, 8H), 2.29 (d, J = 6.6 Hz, 2H), 2.15 (s, 3H), 1.34 (d, J = 7.0 Hz, 3H), 0.94−0.82 (m, 1H), 0.57−0.46 (m, 2H), 0.12 (t, J = 5.1 Hz, 2H). ^{13}C NMR (101 MHz, $CDCl_3$) δ 172.35, 162.50, 141.61, 135.98, 126.82, 118.20, 64.65, 63.51, 53.23, 51.53, 15.35, 12.27, 8.15, 3.70. HRMS (ESI) *m/z*: calcd for $C_{18}H_{28}N_3O_3S$, 352.1689; found 366.1835 $[M + H]^+$. HPLC purity: 99.556%, t_R = 18.690 min.

*Methyl 4-methyl-3-(2-(4-propylpiperazin-1-yl)propanamido)thiophene-2-carboxylate (**AT-16**).* Yield: 74.8%, colorless oil. The preparation of hydrochloride compound was same as **AT**. ^{1}H NMR (400 MHz, $CDCl_3$) δ 9.89 (s, 1H), 7.10 (s, 1H), 3.82 (s, 3H), 3.20 (q, J = 7.0 Hz, 1H), 2.87−2.38 (m, 8H), 2.38−2.28 (m, 2H), 2.14 (d, J = 1.1 Hz, 3H), 1.59−1.44 (m, 2H), 1.33 (d, J = 7.0 Hz, 3H), 0.90 (t, J = 7.4 Hz, 3H). ^{13}C NMR (101 MHz, $CDCl_3$) δ 172.58, 162.71, 141.79, 136.21, 127.02, 118.49, 64.87, 60.67, 53.41, 51.78, 20.07, 15.55, 12.53, 11.99. HRMS (ESI) *m/z*: calcd for $C_{17}H_{28}N_3O_3S$, 354.1846; found 354.1835 $[M + H]^+$. HPLC purity: 98.935%, t_R = 18.446 min.

*Methyl 3-(2-(4-butylpiperazin-1-yl)propanamido)-4-methylthiophene-2-carboxylate (**AT-17**).* Yield: 52.7%, colorless oil. ^{1}H NMR (400 MHz, $CDCl_3$) δ 9.90 (s, 1H), 7.11 (s, 1H), 3.83 (s, 3H), 3.20 (q, J = 7.0 Hz, 1H), 2.96−2.42 (m, 8H), 2.42−2.34 (m, 2H), 2.19−2.10 (m, 3H), 1.56−1.44 (m, 2H), 1.39−1.27 (m, 5H), 0.92 (t, J = 7.3 Hz, 3H). ^{13}C NMR (101 MHz, $CDCl_3$) δ 172.56, 162.73, 141.80, 136.22, 127.03, 118.49, 64.87, 58.47, 53.43, 51.79, 29.05, 20.81, 15.55, 14.07, 12.53. HRMS (ESI) *m/z*: calcd for $C_{18}H_{30}N_3O_3S$, 368.2002; found 368.1991 $[M + H]^+$. HPLC purity: 99.409%, t_R = 19.173 min.

*Methyl 4-methyl-3-(2-(4-phenylpiperazin-1-yl)propanamido)thiophene-2-carboxylate (**AT-18**).* Yield: 60.2%. Grey solid, m.p. 137−138 °C. ^{1}H NMR (400 MHz, $CDCl_3$) δ 10.01 (s, 1H), 7.33−7.27 (m, 2H), 7.13 (d, J = 1.1 Hz, 1H), 7.02−6.94 (m, 2H), 6.91−6.84 (m, 1H), 3.82 (s, 3H), 3.44−3.24 (m, 5H), 2.93−2.71 (m, 4H), 2.19 (d, J = 1.0 Hz, 3H), 1.40 (d, J = 7.0 Hz, 3H). ^{13}C NMR (101 MHz, $CDCl_3$) δ 172.39, 162.78, 151.33, 141.89, 136.16, 129.16, 127.14, 119.76, 118.26, 116.16, 65.02, 51.85, 50.25, 49.36, 15.63, 12.67. HRMS (ESI) *m/z*: calcd for $C_{20}H_{26}N_3O_3S$, 388.1689; found 388.1680 $[M + H]^+$. HPLC purity: 98.645%, t_R = 20.010 min.

Methyl 3-(2-(4-(2-hydroxyethyl)piperazin-*1-yl*)propanamido)-4-methylthiophene- *2-carboxylate (**AT-19**).* Yield: 40.9%, colorless oil. ^{1}H NMR (400 MHz, $CDCl_3$) δ 9.90 (s, 1H), 7.12 (s, 1H), 3.83 (s, 3H), 3.64 (t, J = 5.4 Hz, 2H), 3.21 (q, J = 7.0 Hz, 1H), 2.80−2.55 (m, 10H), 2.18−2.11 (m, 3H), 1.35 (d, J = 7.0 Hz, 3H). ^{13}C NMR (101 MHz, $CDCl_3$) δ 172.54, 162.86, 141.93, 136.27, 127.19, 118.41, 64.96, 59.37, 57.88, 53.13, 51.87, 15.65, 12.72. HRMS (ESI) *m/z*: calcd for $C_{16}H_{26}N_3O_4S$, 356.1639; found 356.1628 $[M + H]^+$. HPLC purity: 99.721%, t_R = 17.124 min.

Methyl 3-(2-(4-(2-methoxyethyl)piperazin-1-yl)propanamido)-4-methylthiophene- *2-carboxylate (**AT-20**)*. Yield: 58.1%, colorless oil. ^{1}H NMR (400 MHz, $CDCl_3$) δ 9.90 (s, 1H), 7.10 (s, 1H), 3.82 (s, 3H), 3.52 (t, J = 5.6 Hz, 2H), 3.34 (s, 3H), 3.19 (q, J = 7.0 Hz, 1H), 2.83−2.46 (m, 10H), 2.14 (s, 3H), 1.32 (d, J = 7.0 Hz, 3H). ^{13}C NMR (101 MHz, $CDCl_3$) δ 172.56, 162.71, 141.79, 136.20, 127.02, 118.47, 70.17, 64.85, 58.91, 57.88, 53.78, 51.77, 15.54, 12.50. HRMS (ESI) *m/z*: calcd for $C_{17}H_{28}N_3O_4S$, 370.1795; found 370.1784 $[M + H]^+$. HPLC purity: 99.002%, t_R = 18.203 min.

*4.3.7. General procedure for the preparation of final compounds **AT-27−30***

The mixture of **AT** (1.0 eq.) in MeOH, NaOH (2.0 eq.) dissolved in H_2O was added, and the mixture was stirred at 50 °C for 2 h. The reaction mixture was concentrated under reduced pressure and diluted with water. After washed by DCM, hydrochloric acid solution (2 mol/L) was used to adjust pH = 7. The mixture was concentrated to give the crude product without further purification. To the above crude (1.0 eq.) in DMF, $NaHCO_3$ (2.0 eq.) and the amine (2.0 eq.) were added and the mixture was stirred at 50 °C for 5 h. After concentrated, the mixture was diluted with, washed with water four times, dried over anhydrous Na_2SO_4, filtered, and concentrated. The residue was purified by chromatography (DCM/MeOH = 40:1) to yield the target products.

*Ethyl 4-methyl-3-(2-(propylamino)propanamido)thiophene-2-carboxylate (**AT-27**)*. Yield: 50.7%, colorless oil. ^{1}H NMR (400 MHz, D_2O) δ 7.44 (d, J = 0.9 Hz, 1H), 4.36−4.21 (m, 3H), 3.15−2.97 (m, 2H), 2.83 (s, 1H), 2.07 (s, 3H), 1.84−1.63 (m, 5H), 1.31 (t, J = 7.1 Hz, 3H), 0.98 (t, J = 7.5 Hz, 3H). ^{13}C NMR (101 MHz, D_2O) δ 169.10, 162.81, 136.84, 136.64, 128.19, 124.62, 62.23, 56.19, 48.18, 19.28, 15.87, 13.52, 12.80, 10.17. HRMS (ESI) *m/z*: calcd for $C_{14}H_{23}N_2O_3S$, 299.1424; found 299.1427 $[M + H]^+$. HPLC purity: 95.393%, t_R = 18.609 min.

*Propyl 4-methyl-3-(2-(propylamino)propanamido)thiophene-2-carboxylate (**AT-28**)*. Yield: 36.3%, colorless oil. ^{1}H NMR (400 MHz, D_2O) δ 7.43 (s, 1H), 4.27 (q, J = 7.0 Hz, 1H), 4.21 (t, J = 6.5 Hz, 2H), 3.15−2.97 (m, 2H), 2.83 (s, 1H), 2.07 (s, 3H), 1.80−1.65 (m, 7H), 0.98 (t, J = 7.4 Hz, 3H), 0.93 (t, J = 7.4 Hz, 3H). ^{13}C NMR (101 MHz, D_2O) δ 169.06, 162.85, 136.86, 136.64, 128.20, 128.16, 124.55, 67.53, 56.21, 48.20, 21.52, 19.29, 15.93, 12.81, 10.18, 9.63. HRMS (ESI) *m/z*: calcd for $C_{15}H_{25}N_2O_3S$, 313.1580; found 313.1580 $[M + H]^+$. HPLC purity: 97.343%, t_R = 19.234 min.

*Butyl 4-methyl-3-(2-(propylamino)propanamido)thiophene-2-carboxylate (**AT-29**)*. Yield: 43.1%, colorless oil. ^{1}H NMR (400 MHz, D_2O) δ 7.31 (d, J = 7.5 Hz, 1H), 4.22−4.09 (m, 3H), 3.06−2.84 (m, 2H), 2.74 (s, 1H), 1.97 (d, J = 1.5 Hz, 3H), 1.70−1.52 (m, 7H), 1.33−1.22 (m, 2H), 0.92−0.84 (m, 3H), 0.83−0.75 (m, 3H). ^{13}C NMR (101 MHz, D_2O) δ 168.99, 162.78, 137.05, 136.65, 128.07, 124.46, 65.80, 56.21, 48.21, 30.05, 19.30, 18.62, 15.96, 12.99, 12.83, 10.20. HRMS (ESI) *m/z*: calcd for $C_{16}H_{27}N_2O_3S$, 327.1737; found 327.1737 $[M + H]^+$. HPLC purity: 98.835%, t_R = 19.758 min.

*Isobutyl 4-methyl-3-(2-(propylamino)propanamido)thiophene-2-carboxylate (**AT-30**)*. Yield: 29.8%, colorless oil. ^{1}H NMR (400 MHz, D_2O) δ 7.48−7.34 (m, 1H), 4.27 (q, J = 6.9 Hz, 1H), 4.09−3.95 (m, 2H), 3.15−2.96 (m, 2H), 2.71 (s, 1H), 2.06 (s, 3H), 2.01−1.92 (m, 1H), 1.81−1.64 (m, 5H), 0.98 (t, J = 7.4 Hz, 3H), 0.91 (d, J = 6.6 Hz, 6H). ^{13}C NMR (101 MHz, D_2O) δ 169.00, 162.69, 136.99, 136.64, 128.10, 124.37, 71.63, 56.21, 48.22, 27.37, 19.29, 18.26, 15.98, 12.83, 10.20. HRMS (ESI) *m/z*: calcd for $C_{16}H_{27}N_2O_3S$, 327.1737; found 327.1739 $[M + H]^+$. HPLC purity: 96.722%, t_R = 17.558 min.

4.4. Cell membrane chromatography

$Na_V1.5/1.7/1.8$-HEK293 cells (Laboratory of Anesthesia and Critical Care Medicine, Chengdu, China) were cultured in DMEM (Gibco, NY, USA) medium containing 10% fetal bovine serum, 100 U/mL penicillin (Gibco, NY, USA) and 100 U/mL (Gibco, NY, USA) streptomycin at 37 °C, 5% CO_2 and saturated humidity. Cells from the exponentially growing culture were harvested with trypsin (Gibco, NY, USA), and a small amount of DMEM medium was used to make single-cell suspension. The cell suspension was centrifuged at 1000 × *g* for 10 min (Beckman coulter, Shanghai, China), poured out the supernatant, suspended with hypotonic solution, and homogenized after ultrasonic membrane breaking 30 min, the suspension was centrifuged at 1000 × *g* for 10 min, the supernatant was centrifuged at 12,000 × *g* at 4 °C, the supernatant was discarded, and the precipitation was re-suspended by adding 5 mL hypotonic solution and centrifuged again. The cell membrane was precipitated and resuscitated with physiological saline precooled by 5 mL to obtain the cell membrane suspension. Then the prepared suspension is adsorbed on the carrier surface to form a stationary cell membrane phase. Next, pellets are suspended in ultra-pure water and packed into a column (10 mm × 2 mm I.D.) (Ripuli, Dalian, China) by using an LC Pump (Agilent, Beijing, China) with ultra-pure water and obtain the cell membrane chromatographic column.

The compound 1 mg/mL was dissolved in methanol, the mobile phase was 0.1% trifluoroacetic acid, the column temperature was 37 °C, the flow rate was 0.2 mL/min, and the chromatographic system was balanced with the mobile phase for 2−3 h. After the baseline was stable, the sample solution 5 μL was injected into the chromatographic system (Agilent, Beijing, China) for analysis and determination, and the time of chromatographic absorption peak was recorded.

4.5. In vivo pharmacodynamics

4.5.1. Animal and treatment

Male Sprague−Dawley rats (Dossy Experimental Animal Company, Chengdu, China) aged 6−8 weeks and weighing 250−300 g were housed at 25 °C with free access to food and water under a 12-h light/12-h dark cycle. ICR mice (Dossy Experimental Animal Company, Chengdu, China) aged 30−40 days and weighing 20−30 g were housed under similar conditions. Animals were acclimated to the experimental environment and experimenter, and handled daily to minimize stress-induced analgesia. Animals were randomly assigned to groups. All animal experiments were performed in compliance with the Agreement of the Experimental Animal Ethics Committee, West China Hospital, Sichuan University.

4.5.2. Cutaneous trunci muscle reflex model

Rats were induced and maintained anesthesia by inhalation of 1%−3% isoflurane (RWD, Shenzhen, China), approximately 6 cm × 6 cm of hair was shaved on the back of the chest and waist with an electric shaver (CHIGO, Ningbo, China), and the skin was sterilized with alcohol cotton swabs and divided into four equal areas. The volume of articaine (62.3 mmol/L) and the new compound (62.3 mmol/L) were respectively injected subcutaneously into the back of the rat to form a visible skin mound and to mark

the outline with a marker, the area within the outline was marked as the area of anesthesia. Note that the needle tip is at a 30-degree angle to the skin when the needle is inserted, and it is withdrawn before injection to avoid accidently entering the blood vessel. During the experiment, a von Frey filament (26 g) (Yuyan Instruments, Shanghai, China) was used as a standardized stimulus to determine pinprick responsiveness (PPR). The anesthetized area was divided into six equal parts, and the skin was acupunctured randomly in each equal part. The penetration depth was approximately 1 mm to see if the rats had PPR. If there is no pain response, 1 point is scored; if there is a pain response, 0 points are scored. The anesthesia expiration time was recorded, and the anesthesia effective time from the anesthesia onset time to the anesthesia expiration time was recorded as the anesthesia duration. The data are expressed as the MPE by average scores. Effectively block was identified as $\geq$50% MPE and completely block was identified as 100% MPE.

4.5.3. *Sciatic nerve block model*

Rats were induced and maintained anesthetized by inhalation of 1%−3% isoflurane, and the sciatic tubercle was shaved with an electric shaver about 2 cm × 2 cm, the skin was sterilized with alcohol cotton swabs, articaine (62.3 mmol/L) or new compound (62.3 mmol/L) was injected near the sciatic nerve. After injection, the rats were placed in a transparent observation cage for observation, and the rats were free to move, eat and drink in the observation cage. The sensory and motor functions of the hind legs were tested every 30 min after drug injection until the test values returned to the baseline levels tested before the experiment. The sensory function was tested by the hotplate test: the hind paw on the injection side was placed on a metal plate at 55 °C (Techman, Chengdu, China), and the measurement index was the time interval (Paw withdrawal latency, PWL), The latency time was measured by a stopwatch when the rat withdrew its paw. To assess the motor block by measuring the extensor postural thrust (EPT), which is a mixed-strength proprioceptive test measured as grams. During testing, the rat is held upright over a digital balance with the hind limbs extended to the platform. A reduction in this force, representing reduced extensor muscle tone, was considered a motor function deficit. We defined a 50% baseline as a recovery indicator, representing muscle recovery, and a difference of more than 1 h between sensory and motor blocks was considered differential in sensory and motor blockades.

4.5.4. *Complete Freund's adjuvant (CFA)-induced chronic inflammation model*

Rats were induced and maintained anesthetized by inhalation of 1%−3% isoflurane, and CFA (complete Freund's adjuvant) (Maokang, Shanghai, China) was injected into the right foot of each rat. After 48 h, it was observed that the soles of the feet were visibly swollen and the withdrawal threshold of the hind paw of the rats was significantly reduced as measured by the electronic Von Frey stimulator (ITCC, Los Angeles, USA). The injected drug was 62.3 mmol/L, the new compound, and the blank control was an equal dose of normal saline. The injection volume for each rat for treatment or control was 0.2 mL and was injected subcutaneously at the swollen site of the rat's foot. The electronic Von Frey stimulator was used to stimulate the side of the foot of the drug-injected rats to observe the effect of local anesthesia. The test was performed every 10 min after the onset of the effect, and the measured value was more than half of the difference between the limb weight and the baseline at the onset of anesthesia, and less than or equal to the value was considered as the failure of anesthesia.

4.5.5. *Incision pain model*

Rats were induced and maintained anesthetized by inhalation of 1%−3% isoflurane. The entire right hind paw was sterilized with 75% ethanol and povidone-iodine; the hairless epidermis, dermis, fascia, and thumb flexor were incised longitudinally with a No. 11 scalpel starting 2 mm from the proximal edge of the heel and the incision was 10 mm in length, after which the muscle was elevated and restored with forceps, and the incision was closed with 3-0 sutures. The injected drug was the new compound and articaine, and the blank control was an equal dose of normal saline. The injection volume of each rat for administration or control was 0.2 mL, and it was injected near the incision site of the rat's plantar foot. The Von Frey stimulator was used to stimulate the lateral sole of the rat to inject the drug, and the effect of local anesthesia was observed. The test was performed every 10 min after the onset of the effect, and the measured value was more than half of the difference between the limb weight and the baseline at the onset of anesthesia, and less than or equal to the value was considered as the failure of anesthesia.

4.5.6. *Oral pain model*

6 SD male rats of similar weight (230−250 g) in each group, rats were induced and maintained anesthetized by inhalation of 1%−3% isoflurane. Prior to the modeling procedure, an inferior alveolar nerve block anesthesia was administered, emulating the prevalent intraoral anesthesia technique used in clinical settings. The precision and effectiveness of this anesthesia method were validated in preliminary experiments (Supporting Information Fig. S1). The following model indirectly evaluated the anesthetic effect of drugs in the oral pain model by reflecting the pain degree of animal food intake, body weight change and the number of autonomous facial grooming. Food intake and weight change were measured by high precision balance (Wensheng, Shanghai, China) for 24 h; facial grooming was recorded by a high-definition camera (EZVIZ, Hangzhou, China) for 1 h after local anesthetic.

4.5.6.1. Dental pulp injury pain model. The mouth opener (RWD, Shenzhen, China) remained open, the tongue was gently retracted using forceps (RWD), the mesial pulp angle of the mandibular first molar was exposed by an electric drill (RWD).

4.5.6.2. Gingival incision pain model. The mouth opener remains open, the tongue gently retracted using forceps. Iodophor disinfected unilateral gum, No. 10 surgical (KYUAN, Suzhou, China) blade was used to cut the gum between the rat's unilateral incisor and molar, and the stripper opened the gingiva, cut and lifted the periosteum, fully exposed the alveolar crest, compressed and stopped the bleeding, the gums were closed with 3-0 sutures (Johnson, Shanghai, China).

4.5.6.3. Tooth extraction pain model. The first molar of the rat was exposed through the opening, and the neck of the first molar of the rat was clamped with curved vascular forceps. The first molar of the rat was dislocated by shaking the first molar to the lip and tongue. The residual root was removed by the dental probe, and then closed the gingiva after compression and hemostasis by 3-0 sutures.

4.5.7. *Toxicity*

4.5.7.1. Systemic toxicity. Systemic toxicity in ICR mice was first determined within an appropriate dose range: mice were

injected into the tail vein of articaine and articaine derivatives (single injection volume 0.2 mL, injection speed is 0.1 mL/s) by 1 mL empty needle. Afterward, the mice were transferred to a transparent observation cage to observe the change in behavioral awareness. If the behavioral activities of the mice stopped and the breathing and heartbeat stopped for more than 5 min, it could be regarded as dead.

Considering that local anesthesia drugs may enter the blood circulation through osmosis and cause systemic toxicity, the systemic toxicity of subcutaneous infiltration anesthesia was determined on the basis of the SD rat model of subcutaneous infiltration anesthesia. Under isoflurane anesthesia, rats were subcutaneously injected with a 1 mL empty needle of articaine and articaine derivatives (single injection volume 1 mL, injection speed is 0.2 mL/s). Afterward, the rats were transferred to a transparent observation cage to observe the changes in behavioral awareness. If the behavioral activities of the rats stopped and the breathing and heartbeat stopped for more than 5 min, they could be regarded as dead. The time of the rat's state of consciousness change and the time of death were recorded. All animals with topical application of drugs without death should be observed continuously for 24 h to observe the distribution of the drug, including whether there is swelling, ulceration, scratches at the injection site, and whether the rats have changes in behavioral consciousness such as convulsions and ataxia. Calculate LD_{50} based on the survival status of rats using the up-and-down procedure[49]. ED_{50} was measured using dose gradient injection of articaine and articaine derivatives in rat subcutaneous infiltration anesthesia model.

4.5.7.2. Local anesthetic toxicity. The local anesthetic toxicity of articaine derivatives and articaine to nerves was assessed by local histological examination of a sciatic nerve block anesthesia model. After the sciatic nerve tissue was anesthetized for 7 and 14 days, the rats were killed by the neck-off method. The sciatic nerve and its surrounding tissues were harvested and stained with hematoxylin-eosin (HE). Inflammatory cells are counted in same sized areas of the tissue (nerve tissue area/the surrounding tissue area was 1:1) by a pathological image analysis software: ImageJ (Version 1.53k).

And after the sciatic nerve tissue was anesthetized for 7 days and 14 days, the rats were killed by the neck-off method. Collect blood samples and important organ samples: heart, liver, kidney; Automatic biochemical analyzer Mindray BS-120 (Mindray, Shenzhen, China) tested blood biochemical indexes (ALT, AST, LDH, α-HBDH, CREA, UREA), and hematoxylin-eosin (HE) stained important organs for pathological analysis. Histological examination was performed by expert pathologists blinded to the experiment and intervention.

4.5.8. Pharmacokinetic

4.5.8.1. Liver microsomal metabolic stability experiment. The compounds to be tested were weighed using an analytical balance, and a storage solution with a concentration of 50 mmol/L (DMSO and acetonitrile mixed at a 1:1 ratio) was prepared for subsequent use. Then, 10 μL of the stock solution of each compound was pipetted and dissolved in 940 μL of phosphate buffer. Subsequently, 50 μL of solution A and 10 μL of solution B were added to the mixture, followed by the addition of 50 μL of the liver microsome incubation system (PrimeTox, Wuhan, China). Each compound was tested in three parallel groups and incubated in a water bath at 37 °C. At each time point, 100 μL of the incubation solution was retrieved from the tube, and 300 μL of acetonitrile was added to precipitate proteins. The solution was vortexed for 1 min and then centrifuged at 12,000 rpm for 10 min. After centrifugation, 100 μL of the supernatant was collected and centrifuged again at the same speed for 10 min. The peak areas of the corresponding mass spectra were integrated using UPLC−MS/MS (Agilent, Beijing, China), and the remaining percent of compound concentrations at each time point was calculated based on the 0 min peak area. Following data collection, the metabolic half-life was calculated using GraphPad software. The liver enzyme incubation system consisted of liver microsomes (0.5 mg/mL), incubation buffer (100 mmol/L phosphate buffer, pH 7.4), the compound to be tested (1 mmol/L), an incubation volume of 0.2 mL, and incubation times of 0, 15, 30, 60, 120, and 180 min, respectively.

4.5.8.2. Pharmacokinetics (PK) study. Three male SD rats received subcutaneous injections of **AT-17** (62.3 mmol/L). Blood samples were collected *via* the jugular vein at 5, 15, 30 min, 1, 2, 4, 6, 8, 12, and 24 h after administration, followed by centrifugation at 6000 rpm for 3 min to separate plasma, which was then stored at −20 °C until analyzed. The plasma concentrations of each animal at each time point were determined using a Triple Quad 5500+ (SCIEX, Shanghai, China) LC−MS/MS system, with Turbo Spray ion source in positive ion mode and multiple reaction monitoring scan mode. The resulting data were analyzed using a non-compartmental model in WinNolin software to calculate pharmacokinetic parameters.

4.6. Biological experiments

4.6.1. Cell culture and reagents

DRG neurons from male rats weighing 180−200 g were dissociated and cultured as described previously. In brief, rats were sacrificed by the spinal cord dislocation method. Then, ganglia were quickly excised and placed in ice-cold Hanks' Balanced Salt Solution (HBSS; Gibco, NY, USA). After removing the connective tissue gently, the ganglia were sequentially digested with 2 mL collagenase IV (2 mg/mL) followed by 2 mL trypsin (10 mg/mL) for 30 min in an incubator. After termination of digestion *via* fetal bovine serum (FBS; cornin, NY, USA), DRG neurons suspension was obtained by filtration. Then, cells were inoculated in petri dishes pre-treated with poly-L-lysine (Sigma−Aldrich, St. Louis, MO, USA) at 37 °C for 1 h. DRG neurons were grown in Neurobasal (Gibco) supplemented with 10% of FBS, 1% penicillin-streptomycin solution (Gibco) and B27 supplement (Thermo Fisher Scientific, MA, USA), PC12 cells were obtained from Conservation Genetics CAS Kunming Cell Bank (No. KCB200735YJ). Cells were cultured in the F12K medium (Gibco) supplemented with 10% horse serum (Gibco) and 5% FBS. To induce their differentiation, PC12 cells were poly-L-lysine-coated plates in the medium supplemented with mouse β-NGF (50 ng/mL; Sino biological, Beijing, China).

Cells were cultured in the MEM and F12 medium (Gibco) supplemented with 10% FBS, 1% Gluta-max (Invitrogen, CA, USA), 1% sodium pyruvate (Invitrogen) and 1% NEAA (Invitrogen).

RAW 264.7 cells were obtained from State Key Laboratory of Oral Disease, Sichuan University. Cells were cultured in DMEM medium (Gibco) containing 10% FBS (Gibco).

All cells were maintained at 37 °C in a humidified atmosphere with 5% CO_2.

4.6.2. Electrophysiology

Whole-cell mode voltage clamp detection: Microelectrode resistance 3−4 MΩ. The in-electrode liquid (K-gluconate 130 mmol/L, NaCl 10 mmol/L, $MgCl_2 \cdot 6H_2O$ 1.2 mmol/L, $CaCl_2$ 2 mmol/L, EGTA 5 mmol/L, HEPES 10 mmol/L, glucose 7.5 mmol/L). Adjust pH to 7.35−7.45 with 1 mol/L KOH. For action potential recording, the electrode fluid contained 136 mmol/L glucose, 10 mmol/L NaCl, 1 mmol/L $MgCl_2$, 10 mmol/L EGTA, 10 mmol/L HEPES, and 2 mmol/L Mg-ATP, adjusted to pH 7.3 with KOH. The outer solution contained 140 mmol/L NaCl, 5 mmol/L KCl, 2 mmol/L $CaCl_2$, 1 mmol/L $MgCl_2$, 10 mmol/L HEPES, and 10 mmol/L glucose, adjusted to a pH of 7.3 with NaOH. The osmotic pressure of all solutions was 300−330 mOsm. All records were taken at room temperature. In voltage clamp mode (clamp potential −70 mV), the voltage was depolarized from −70 to 0 mV, and the stimulation time was 50 ms. The sodium current track was recorded and the magnitude of the sodium current was detected. The I/V curve of the effect of the drug on sodium current was detected by applying voltage clamp mode to cells from −90 to +40 mV in steps of 10 mV for each step and stimulating 50 ms. In the current clamp mode, the cells were given step current from 0 pA to +300 pA, each step was 10 pA, and stimulated for 600 ms. The intensity of the action potential base of the neurons was detected, and the number and amplitude of the evoked neuron generated action potential under the stimulation of twice the intensity of the base were counted. The recorded signal was amplified by a Multi Clamp 700B amplifier, filtered at 10 kHz, and converted by an Axon Digidata 1440 A digital-to-analog/analog-to-digital converter at a sampling frequency of 10−20 kHz.

Whole-cell model current clamp detection: When the action potential was recorded, the extracellular fluid contained 140 mmol/L NaCl. 3.5 mmol/L KCl; 2 mmol/L $CaCl_2 \cdot 2H_2O$; 2 mmol/L $MgCl_2 \cdot 6H_2O$; 10 mmol/L HEPES; 10 mmol/L D-glucose; 1.25 mmol/L $NaH_2PO_4 \cdot 2H_2O$. The liquid in the electrode contains 140 mmol/L KCl; 1 mmol/L $CaCl_2$; 1 mmol/L $MgCl_2$; 2 mmol/L Na_2ATP; 10 mmol/L EGTA; 5 mmol/L HEPES, KOH to pH 7.2. After the cell membrane was broken, the current clamp mode was changed, and the membrane potential should be lower than −40 mV. Current pulses increase from 0 to 1000 pA in 5 pA increments and last for 200 ms until at least one action potential is triggered. The threshold current triggering the action potential is denoted as the base intensity. The injection of a depolarization current with twice the base intensity induced the firing behavior of the neurons.

4.6.3. Molecular dynamics simulation

The study utilized molecular dynamics (MD) simulation to investigate the binding interactions between **AT**, **AT-17**, and voltage-gated sodium channels ($Na_V1.7$ and $Na_V1.8$). The focus was on analyzing their binding patterns, dynamic binding processes, and the energy determinants of amino acids. The crystal structures of $Na_V1.7$ complexed with IN2 (PDB ID: 7xmf) and $Na_V1.8$ complexed with A-803467 (PDB ID: 7we4) from the Protein Data Bank were used as references due to their similarity to **AT** and **AT-17** binding cavities, and the binding site for local anesthetics in $Na_V1.7$ and $Na_V1.8$ was found to be located within the inner lumen of the channel pore. CDOCKER docking program was used for docking to obtain a reasonable initial complex conformation in the Discovery Studio 2019 software package. The protein-ligand complex systems were conveniently constructed by CHARMM-GUI[50], and models of the voltage-gated sodium channels and the ligands were constructed and optimized using the CHARMM and CGenFF force fields, respectively[51,52], The system was solvated with the TIP3 water model and neutralized with potassium and chloride ions. Prior to the production simulation, a steepest descent algorithm was employed to minimize the system for 100 ps in order to eliminate any unnatural collisions. Subsequently, a 250 ps equilibration process was conducted, gradually releasing the scaling restraint until the force was fully removed. The MD simulation was performed under NPT conditions at a temperature of 303.15 K and a pressure of 1 atm, using a time step of 2 fs and constraining bonds involving hydrogen atoms with the LINCS algorithm. The particle mesh Ewald (PME) method was used for calculating electrostatic interactions. Finally, a 200 ns MD simulation was carried out, and the root mean square deviation (RMSD) per residue was calculated based on all atoms after trajectory alignment. To estimate the interaction-free energies, Molecular Mechanics Poisson-Boltzmann Surface Area (MM-PBSA) and Molecular Mechanics with Generalized Born Surface Area (MM-GBSA), were employed. The calculations were performed locally, and the binding free energy of the complex was determined using the "gmx_mmpbsa" tool by analyzing 100 frames extracted from the last 10 ns of the equilibrium stage MD trajectory[53]. All simulations were performed with the Gromacs software package, version 2021.6[54]. Detailed protein-ligand interactions were plotted in Chimera 1.13[55].

4.6.4. qRT-PCR

Total RNA of cells was extracted *via* Trizol. The reverse transcription was carried out following the manufacturer's procedure using HiScript III 1st Strand cDNA Synthesis Kit (+gDNA wiper) (Vazyme, R312). Then qRT-PCR was performed with on ABI PRISM 7900 sequence detection system. Reaction system: 12 μL DEPC water, 4 μL 5 × BlazeTaq qPCR Mix, 1 μL Forward Primer (10 μmmol/L), 1 μL Reverse Primer (10 μmmol/L), 2 μL template cDNA, final volume was 20 μL. Reaction conditions: 95 °C 30 s → (95 °C 10 s → 60 °C 30 s) × 40 cycles. Specific primers of each gene for qRT-PCR were shown as followed. All experiments were repeated three times at least and the relative expressions of detected genes were calculated *via* $2^{-\Delta\Delta CT}$ method.

Primers of genes for qRT-PCR:

Gene	Forward primer	Reverse primer
IL1β	CACCTCTCAAGCA GAGCACAG	GGGTTCCATGGTGAA GTCAAC
TNF-α	CAAGGAGGAGAAG TTCCCAA	TGATCTGAGTGTGAG GGTCTG
IL6	CTGGTCTTCTGGAG TTCCGT	TGGTCTTGGTCCTTAG CCAC
GAPDH	ACAGCCGCATCTTC TTGTGCAGTG	GGCCTTGACTGTGCCG TTGAATTT

4.6.5. ELISA

IL1β, TNF-α and IL6 secretion were quantified using respective ELISA kits (Neobioscience, China) following the manufacturer's instructions.

4.6.6. Westing bolt

Total proteins of tissue specimens were prepared *via* RIPA lysis buffer. Next, proteins were separated through sodium dodecyl sulfate−polyacrylamide gel electrophoresis. Then, gel was transferred onto a PVDF membrane (Millipore, Boston, MA, USA).

After blocked in 5% defatted milk for 2 h, membranes were incubated with specific primary antibody overnight at 4 °C. Primary antibodies were listed as follows: anti-Nlrp3 (1:1000, mouse; Adipogen, Stahl, Switzerland), anti-caspase-1 (1:1000, mouse; Adipogen), anti-ASC (1:25,000, rabbit; Proteintech, Chicago, USA), anti-GSDMD (1:500 mouse; Huabio, Hangzhou, China) and anti-GAPDH (1:15,000, rabbit; Signalway, Beijing, USA). After incubating goat anti-rabbit or goat anti-mouse secondary antibody (MultiSciences, Hangzhou, China), membranes with target protein incubated with the chemiluminescence reagent (Yamei Biotechnology, Shanghai, China) were visualized *via* ChemiDoc XRS + System (Bio-Rad, Hercules, CA, USA).

4.6.7. NLRP3 inflammasome activation

NLRP3 inflammasome activation was detected by immunofluorescence ASC antibodies. Briefly, cells were seeded on the poly-L-lysine-coated slides. After fixed with 3% paraformaldehyde for 15 min and permeabilized with 0.5% triton X-100 for 15 min, the slides were blocked with 5% BSA for 2 h at room temperature and incubated with ASC antibodies (1:200; Proteintech) overnight at 4 °C. Afterwards, the slides were incubated with the secondary antibodies (1:500) for 1 h at room temperature in the dark. After incubated with DAPI, ASC specks were visualized *via* fluorescence microscope (Laika, Wetzlar, German).

4.6.8. Immunofluorescence

Cells were seeded on the poly-L-lysine-coated slides. For 8-ohdg staining, cells were firstly incubated with MitoTracker Deep Red (500 nmol/L; Beyotime, Shanghai, China) at 37 °C for 20 min, fixed with methanol and then treated with 0.2% Triton X-100 (Sigma−Aldrich, MO, USA) to increase cell membrane penetrability. Cells were incubated with ASC (1:200; Proteintech, Chicago, USA), dsDNA (1:50; Santa Cruz, USA), TOMM20 (1:250; Abcam, Boston, USA), 8-ohdg (1:250; Bioss, Beijing, China) at 4 °C overnight and then incubated with goat anti-rabbit IgG H&L/AF647 secondary antibodies (1:500; Bioss), goat anti-mouse IgG H&L/AF488 secondary antibodies (1:500; Bioss) for 1 h at room temperature. Nuclei were stained with 4′,6-diamidino-2-phenylindole (DAPI) (Boster, Wuhan, China) for 20 min. Immunofluorescence images were acquired by confocal laser scanning microscopy.

4.7. Statistics

Data are presented as means ± SEM. Clinical scoring of wounds is presented as medians. Differences in the mean between the two groups were analyzed using Student's *t*-test for normally distributed data. To compare means between more than two groups, a one-way analysis of variance (ANOVA) with *post hoc* (Tukey) for normally distributed data. Statistical analysis, as indicated in each figure legend, was performed using GraphPad Prism software v9.4.1. Data are mean ± SEM; $^{*}P < 0.05$, $^{**}P < 0.01$, $^{***}P < 0.001$ and $^{****}P < 0.0001$. $P > 0.05$ was considered to be statistically significant.

Acknowledgments

This study was supported by the National Natural Science Foundation of China (82273784, China); the Research and Develop Program, West China Hospital of Stomatology Sichuan University (RD-03-202004, China); the 1.3.5 Project for Disciplines of Excellence, West China Hospital, Sichuan University (ZYYC 21002, ZYGD23025, China); the Clinical Research Innovation Project, West China Hospital, Sichuan University (2019 HXCX006, China); the Science and Technology Major Project of Tibetan Autonomous Region of China (XZ202201ZD0001G, China); the Sichuan Science and Technology Program (2023 ZYD0168, China).

Author contributions

Conceptualization: Xianggen Liu, Ling Ye, Jin Liu, Xinhua Liang, Bowen Ke; Designed and performed research: Yihang Hao, Wenrui Gai, Wencheng Liu; Assisted in the experiments: Rongjia Shi, Yongzhen Tan, Ting Kang, Ao Hai, Yi Zhao, Yaling Tang; Data analysis: Haofan Wang, Wencheng Liu, Shilong Hu, Xianghua Yu; Manuscript writing, review and editing: Yihang Hao, Haofan Wang, Xianggen Liu, Wenrui Gai, Zhuang Miao, Yu Gan, Yihang Fu, Xinhua Liang, Bowen Ke. All authors critically reviewed and approved the manuscript.

Conflicts of interest

The authors declare no conflicts of interest.

Appendix A. Supporting information

Supporting information to this article can be found online at https://doi.org/10.1016/j.apsb.2024.01.019.

References

1. Sun J, Zhong H, Wang K, Li N, Chen L. Gains from no real pains: where 'fair trial strategy' stands in the development of multi-target ligands. *Acta Pharm Sin B* 2021;**11**:3417−32.
2. Li X, Li X, Liu F, Li S, Shi D. Rational multitargeted drug design strategy from the perspective of a medicinal chemist. *J Med Chem* 2021;**64**:10581−605.
3. Zhou J, Jiang X, He S, Jiang H, Feng F, Liu W, et al. Rational design of multitarget-directed ligands: strategies and emerging paradigms. *J Med Chem* 2019;**62**:8881−914.
4. Sousa T, Correia J, Pereira V, Rocha M. Generative deep learning for targeted compound design. *J Chem Inf Model* 2021;**61**:5343−61.
5. Grisoni F, Huisman BJH, Button AL, Moret M, Atz K, Merk D, et al. Combining generative artificial intelligence and on-chip synthesis for *de novo* drug design. *Sci Adv* 2021;**7**:eabg3338.
6. Glogg RY, Timonina-Farkas A, Seifert RW. Modeling and mitigating supply chain disruptions as a bilevel network flow problem. *Comput Manag Sci* 2022;**19**:395−423.
7. Schneider P, Walters WP, Plowright AT, Sieroka N, Listgarten J, Goodnow Jr RA, et al. Rethinking drug design in the artificial intelligence era. *Nat Rev Drug Discov* 2020;**19**:353−64.
8. Kingma DP, Welling MJC. Auto-encoding variational bayes. *arXiv* 2013. Available from: https://arxiv.org/abs/1312.6114.
9. Goodfellow I, Pouget-Abadie J, Mirza M, Xu B, Warde-Farley D, Ozair S, et al. Generative adversarial networks. *Commun ACM* 2020;**63**:139−44.
10. Bengio E, Jain M, Korablyov M, Precup D, Bengio Y. Flow network based generative models for non-iterative diverse candidate generation. *arXiv* 2021. Available from: https://arxiv.org/abs/2106.04399.
11. Ho J, Jain A, Abbeel P. Denoising diffusion probabilistic models. *arXiv* 2020. Available from: https://arxiv.org/abs/2006.11239.
12. Ekins S, Puhl AC, Zorn KM, Lane TR, Russo DP, Klein JJ, et al. Exploiting machine learning for end-to-end drug discovery and development. *Nat Mater* 2019;**18**:435−41.

13. Wang J, Hsieh CY, Wang M, Wang X, Wu Z, Jiang D, et al. Multi-constraint molecular generation based on conditional transformer, knowledge distillation and reinforcement learning. *Nat Mach Intell* 2021;**3**:914−22.
14. Mahmood O, Mansimov E, Bonneau R, Cho K. Masked graph modeling for molecule generation. *Nat Commun* 2021;**12**:3156.
15. Strobl MAR, Barker D. On simulated annealing phase transitions in phylogeny reconstruction. *Mol Phylogenet Evol* 2016;**101**:46−55.
16. Nagendrababu V, Duncan HF, Whitworth J, Nekoofar MH, Pulikkotil SJ, Veettil SK, et al. Is articaine more effective than lidocaine in patients with irreversible pulpitis?. An umbrella review. *Int Endod J* 2020;**53**:200−13.
17. Larocca de Geus J, Nogueira da Costa JK, Wambier LM, Maran BM, Loguercio AD, Reis A. Different anesthetics on the efficacy of inferior alveolar nerve block in patients with irreversible pulpitis: a network systematic review and meta-analysis. *J Am Dent Assoc* 2020;**151**:87−97.e4.
18. St George G, Morgan A, Meechan J, Moles DR, Needleman I, Ng YL, et al. Injectable local anaesthetic agents for dental anaesthesia. *Cochrane Database Syst Rev* 2018;**7**:Cd006487.
19. Shetty SS, Jayaraj R, Riahi SM, Parthipady K. Articaine efficacy. *J Am Dent Assoc* 2021;**152**:341.
20. Maruthingal S, Mohan D, Maroli RK, Alahmari A, Alqahtani A, Alsadoon M. A comparative evaluation of 4% articaine and 2% lidocaine in mandibular buccal infiltration anesthesia: a clinical study. *J Int Soc Prev Community Dent* 2015;**5**:463−9.
21. Liu X, Li P, Meng F, Zhou H, Zhong H, Zhou J, et al. Simulated annealing for optimization of graphs and sequences. *Neurocomputing* 2021;**465**:310−24.
22. Jin W, Barzilay R, Jaakkola TJA. Junction tree variational autoencoder for molecular graph generation. *arXiv* 2018. Available from: https://arxiv.org/abs/1802.04364.
23. You J, Liu B, Ying R, Pande VS, Leskovec J. Graph convolutional policy network for goal-directed molecular graph generation. *arXiv* 2018. Available from: https://arxiv.org/abs/1806.02473.
24. Zhang J, Jade Sanderson AC. Adaptive differential evolution with optional external archive. *IEEE Trans Evol Comput* 2009;**13**:945−58.
25. Dossetter AG, Griffen EJ, Leach AG. Matched molecular pair analysis in drug discovery. *Drug Discov Today* 2013;**18 15**−**16**:724−31.
26. Zang C, Wang F. Moflow: an invertible flow model for generating molecular graphs. *arXiv* 2020. Available from: https://arxiv.org/abs/2006.10137.
27. Shi C, Xu M, Zhu Z, Zhang W, Zhang M, Tang JJA. Graphaf: a flow-based autoregressive model for molecular graph generation. *arXiv* 2020. https://arxiv.org/abs/2001.09382.
28. Wang K, Xiao J, Liu X, Jiang Z, Zhan Y, Yin T, et al. Aicd: an integrated anti-inflammatory compounds database for drug discovery. *Sci Rep* 2019;**9**:7737.
29. Yang K, Swanson K, Jin W, Coley C, Eiden P, Gao H, et al. Analyzing learned molecular representations for property prediction. *J Chem Inf Model* 2019;**59**:3370−88.
30. Xiong G, Wu Z, Yi J, Fu L, Yang Z, Hsieh C, et al. Admetlab 2.0: an integrated online platform for accurate and comprehensive predictions of admet properties. *Nucleic Acids Res* 2021;**49**:W5−w14.
31. Hou X, Wang S, Zhang T, Ma J, Zhang J, Zhang Y, et al. Recent advances in cell membrane chromatography for traditional Chinese medicines analysis. *J Pharm Biomed Anal* 2014;**101**:141−50.
32. Huang X, Kong L, Li X, Chen X, Guo M, Zou H. Strategy for analysis and screening of bioactive compounds in traditional Chinese medicines. *J Chromatogr, B: Anal Technol Biomed Life Sci* 2004;**812**:71−84.
33. Yuan BX, Hou J, He LC, Yang GD. Evaluation of drug-muscarinic receptor affinities using cell membrane chromatography and radioligand binding assay in Guinea pig jejunum membrane. *Acta Pharmacol Sin* 2005;**26**:113−6.
34. Shearer J, Castro JL, Lawson ADG, MacCoss M, Taylor RD. Rings in clinical trials and drugs: present and future. *J Med Chem* 2022;**65**:8699−712.
35. da Silva GHR, Mendes LF, de Carvalho FV, de Paula E, Duarte IF. Comparative metabolomics study of the impact of articaine and lidocaine on the metabolism of sh-sy5y neuronal cells. *Metabolites* 2022;**12**:581.
36. Tzeng JI, Pan HJ, Liu KS, Chen YW, Chen YC, Wang JJ. Epinephrine as adjuvant for propranolol produces a marked peripheral action in intensifying and prolonging analgesia in response to local dorsal cutaneous noxious pinprick in rats. *Eur J Pharmacol* 2014;**740**:565−9.
37. Markova L, Cvetko E, Ugwoke CK, Horvat S, Umek N, Stopar Pintarič T. The influence of diabetic peripheral neuropathy on the duration of sciatic nerve block with 1.3% liposomal bupivacaine and 0.25% bupivacaine hydrochloride in a mouse model. *Pharmaceutics* 2022;**14**:1824.
38. Li W, Yan Y, Chang Y, Ding L, Liu H, You Q. Synthesis, sciatic nerve block activity evaluation and molecular docking of fluoro-substituted lidocaine analogs as local anesthetic agents. *Med Chem Res* 2019;**28**:1783−95.
39. Li W, Ding L, Liu H-M, You Q. Synthesis, biological evaluation, and molecular docking of ropivacaine analogs as local anesthetic agents. *Med Chem Res* 2018;**27**:954−65.
40. Chowdhury S, Liu S, Cadieux JA, Hsieh T, Chafeev M, Sun S, et al. Tetracyclic spirooxindole blockers of hnav1.7: activity *in vitro* and in cfa-induced inflammatory pain model. *Med Chem Res* 2013;**22**:1825−36.
41. Dong S, Zhang K, Shi Y. Carbenoxolone has the potential to ameliorate acute incision pain in rats. *Mol Med Rep* 2021;**24**:520.
42. Yu P, Zhang X, Liu N, Tang L, Peng C, Chen X. Pyroptosis: mechanisms and diseases. *Signal Transduct Targeted Ther* 2021;**6**:128.
43. Huang Y, Xu W, Zhou R. Nlrp3 inflammasome activation and cell death. *Cell Mol Immunol* 2021;**18**:2114−27.
44. Kwon EB, Li W, Kim YS, Kim B, Chung HS, Go Y, et al. Vitisin b inhibits influenza a virus replication by multi-targeting neuraminidase and virus-induced oxidative stress. *Acta Pharm Sin B* 2023;**13**:174−91.
45. Li W, Cai H, Ren L, Yang Y, Yang H, Liu J, et al. Sphingosine kinase 1 promotes growth of glioblastoma by increasing inflammation mediated by the NF-κB/IL-6/STAT3 and JNK/PTX3 pathways. *Acta Pharm Sin B* 2022;**12**:4390−406.
46. Siebrands CC, Friederich P. Inhibition of herg channels by the local anaesthetic articaine. *Eur J Anaesthesiol* 2007;**24**:148−53.
47. Huang X, Jin X, Huang G, Huang J, Wu T, Li Z, et al. Structural basis for high-voltage activation and subtype-specific inhibition of human Na(v)1.8. *Proc Natl Acad Sci U S A* 2022;**119**:e2208211119.
48. Zhang J, Shi Y, Huang Z, Li Y, Yang B, Gong J, et al. Structural basis for Nav1.7 inhibition by pore blockers. *Nat Struct Mol Biol* 2022;**29**:1208−16.
49. Bruce RD. An up-and-down procedure for acute toxicity testing. *Fund Appl Toxicol* 1985;**5**:151−7.
50. Jo S, Kim T, Iyer VG, Im W. Charmm-gui: a web-based graphical user interface for charmm. *J Comput Chem* 2008;**29**:1859−65.
51. Klauda JB, Venable RM, Freites JA, O'Connor JW, Tobias DJ, Mondragon-Ramirez C, et al. Update of the charmm all-atom additive force field for lipids: validation on six lipid types. *J Phys Chem B* 2010;**114**:7830−43.
52. Best RB, Zhu X, Shim J, Lopes PE, Mittal J, Feig M, et al. Optimization of the additive charmm all-atom protein force field targeting improved sampling of the backbone φ, ψ and side-chain $\chi(1)$ and $\chi(2)$ dihedral angles. *J Chem Theor Comput* 2012;**8**:3257−73.
53. Valdés-Tresanco MS, Valdés-Tresanco ME, Valiente PA, Moreno E. Gmx_mmpbsa: a new tool to perform end-state free energy calculations with gromacs. *J Chem Theor Comput* 2021;**17**:6281−91.
54. Abraham MJ, Murtola T, Schulz R, Páll S, Smith JC, Hess B, et al. Gromacs: high performance molecular simulations through multi-level parallelism from laptops to supercomputers. *SoftwareX* 2015;**1**−**2**:19−25.
55. Pettersen EF, Goddard TD, Huang CC, Couch GS, Greenblatt DM, Meng EC, et al. Ucsf chimera—a visualization system for exploratory research and analysis. *J Comput Chem* 2004;**25**:1605−12.